Improvements in Typhoon Forecasts with Assimilated GPS Occultation Refractivity

CHING-YUANG HUANG

Department of Atmospheric Sciences, National Central University, Chung-Li, Taiwan

YING-HWA KUO

University Corporation for Atmospheric Research, and National Center for Atmospheric Research, Boulder, Colorado

SHU-HUA CHEN

Department of Land, Air, and Water Resources, University of California, Davis, Davis, California

FRANCOIS VANDENBERGHE

National Center for Atmospheric Research, Boulder, Colorado

(Manuscript received 17 May 2004, in final form 9 February 2005)

ABSTRACT

In this study, the fifth-generation Pennsylvania State University–National Center for Atmospheric Research Mesoscale Model (MM5) with three-dimensional variational data assimilation (3DVAR) is utilized to investigate influences of GPS occultation refractivity on simulations of typhoons past Taiwan. Two recent cases were simulated, including Typhoon Nari in September 2001 and Typhoon Nakri in July 2002. The GPS observation data are taken from the Challenging Minisatellite Payload for Geophysical Research and Application (CHAMP) and Satélite de Aplicaciones Científicas-C (SAC-C) satellites that provide several retrieved refractivity profiles in the simulated domain near the initialization time. Through 3DVAR, the observed refractivity can be quickly ingested into the model initial conditions to recover the information over the ocean.

The initial moisture increments from ingested GPS refractivity soundings exhibit a maximum magnitude of about 1.5 g kg^{-1} associated with temperature increments of generally less than 0.2°C. The differences between the model local refractivity and the observed refractivity are less than 3% with a maximum magnitude of about 10 units. Pronounced increments from an occultation point are found within an influential radius of 500–600 km only. For the simulation without the assimilation of GPS refractivity (the no-GPS run), the simulated Typhoon Nari coherently moves southwestward toward Taiwan early in the simulation but then exhibits a westward track along the northwest of Taiwan after landfall. With GPS refractivity assimilated, the simulated westward track in the no-GPS run is closer to the west coast. During landfall, the cloud convection associated with the intense vortex core encounters the Central Mountain Range (CMR) and produces torrential rainfalls along its northwestern slope. Both the GPS run and the no-GPS run capture the observed feature of very intense rainfall over the southwestern slope base of the CMR later in the simulation, while the intensity as well as the track is improved in the GPS run. In the other case (Nakri), the simulated rainfall distributions, in general, are similar for both the GPS run and the no-GPS run; however, the GPS run exhibits a more pronounced low to the southeast of Taiwan, which results in more intense rainfall in the northeast of Taiwan as observed. Both GPS runs for Nari and Nakri show improved skills in 24-h accumulated rainfall prediction, in particular, at later stages, as supported by higher threat scores and smaller root-mean-square errors against observations over the island. This positive impact can be attributed largely to the fact that the accumulative effects from assimilation of initial GPS refractivity soundings are instrumental to model performance.

A cycling 3DVAR scheme is also explored in the simulation for Nari to investigate the impact of complementary NASA Quick Scatterometer (QuikSCAT) near-surface wind observations on model prediction. When such observed near-surface wind is assimilated into reinitialization at a later integration time, the track prediction is further improved and thus the prediction for accumulated rainfall is improved as well.

Corresponding author address: Prof. Ching-Yuang Huang, Dept. of Atmospheric Sciences, National Central University, Chung-Li 32001, Taiwan.
E-mail: hcy@atm.ncu.edu.tw

1. Introduction

Three-dimensional variational data assimilation (3DVAR) analysis utilizes observations as well as background analyses near the initial time of model integration to minimize a cost function with respect to the analysis. The 3DVAR method does not require integration of both the forward model and the adjoint model, as does 4DVAR (Zou et al. 1997), and thus greatly simplifies the filtering processes with ingestion of various observations (Courtier et al. 1998; Rabier et al. 1997; Vandenberghe and Kuo 1999). Another advantage of 3DVAR, as compared to 4DVAR, is that it is handy for setting up multiple nested domains suitable for simulations of phenomena at small scales. With more and more unconventional data (including measurements from satellite, radar, and other remote sensors) being available, ingestion of these data into NWP models is believed to be a high priority for improving NWP. In this study, a fifth-generation Pennsylvania State University–National Center for Atmospheric Research (Penn State–NCAR) Mesoscale Model (MM5) 3DVAR scheme is used to incorporate recent GPS sounding observations and to explore their impacts on nested simulations of typhoons past Taiwan.

GPS sounding observations are limb measurements from global occultation of small low-earth-orbit (LEO) satellites. As these LEO satellites rise and set relative to the GPS satellites, the delayed phase of the GPS-relayed dual-frequency signals can be detected for analysis. This radio occultation technique (GPS/MET) has an advantage on the measurability of all weather conditions with rather even global coverage over land and ocean. Through existing retrieval algorithms, the received signals then can be converted to bending angles or refractivities with assumptions of different degrees of freedom. Such LEO satellites include the Global Positioning System/Meteorological Applications MicroLab I, which was launched in 1995 by the University Corporation for Atmospheric Research (UCAR), and the present Challenging Minisatellite Payload for Geophysical Research and Application (CHAMP, Germany) and Satélite de Aplicaciones Científicas-C (SAC-C, Argentina). The two operating satellites, CHAMP and SAC-C, may collectively receive about 350 occultation events daily. The soon-to-be-launched third Republic of China Remote Sensing Satellite (ROCSAT-3) is a new joint project between the United States and Taiwan as part of the Constellation Observing Systems for Meteorology, Ionosphere and Climate (COSMIC) program, will launch six LEO satellites in late 2005 that can take about 2500–3000 daily measurements for real-time applications. The details of COSMIC and the data quality of the different occultation observations have been discussed in Anthes et al. (2000). Ware et al. (1996) reported that dry temperature retrieved from occultation observations of GPS/MET has nearly the same accuracy as that of rawinsonde soundings nearby. Thus, the GPS data, to some extent, may compensate for unavailable conventional soundings in data-sparse oceanic and polar regions. The assimilation of the GPS/MET data and their impact on weather prediction have been explored in numerical modeling studies (Kuo et al. 1997; Zou et al. 1999, 2000; Liu and Zou 2003), none of which is, however, related to simulations of typhoons.

The data from GPS occultation observations have various forms for assimilation, from original excess phases to retrieved moisture and/or temperature profiles. GPS refractivity is an intermediate product from an Abel transform of bending angles defined for each incident ray through its perigee point. The Abel transform requires an assumption on spherical symmetry that is less applicable to the lower atmosphere where more weather activities and stronger horizontal density gradients tend to exist. As a result, the Abel-retrieved refractivity is often referred to as nonlocal refractivity, due to the retrieval along the ray with spherical symmetry. With this a priori assumption, the application of refractivity thus is more limited than bending angles.

Use of the ray-tracing method to solve for bending angles, however, takes expensive computation time and assimilation into the model is at a cost that is at least one to two orders of magnitude larger than the assimilation of refractivity (Zou et al. 1999, 2000; Kuo et al. 2000). Despite the relative simplicity of the assimilation of refractivity, Kuo et al. (1997) showed some positive impact of the GPS-retrieved refractivity on the prediction of an extratropical cyclone based on observing system simulation experiments (OSSEs) in which the GPS observations are generated by the applied model itself. Also based on an OSSE, Zou et al. (1995) adopted a 4DVAR approach with the adjoint adiabatic MM5 to assimilate GPS refractivity. Their results also showed promising improvement as the GPS refractivity data were assimilated. On the other hand, Liu and Zou (2003) found improvement in global prediction when 837 bending-angle soundings from GPS/MET were assimilated into the National Centers for Environmental Prediction (NCEP) Global Spectral Model. Thus, assimilations of GPS occultation data in various forms, despite different advantages, have their own values on NWP as discussed by Kuo et al. (2000).

As model grid resolution is getting higher (e.g., in mesoscale models) to account for strong horizontal gradients, the nonlinear operator for bending angle will be

more susceptible to small variations in ray-tracing trajectory that may result in slow convergence of the functional minimization. Direct assimilation of bending angles in mesoscale models also needs to simulate ray tracing within limited horizontal extents and the associated lateral boundary conditions may not be well posed. At present, the assimilation of GPS occultation refractivity remains plausible and feasible in fact for high-resolution mesoscale modeling with compromises between accuracy and efficiency.

In this study, the newly developed assimilation module for GPS refractivity in an MM5 3DVAR analysis is utilized to incorporate these data available from CHAMP and SAC-C satellites. Two recent typhoon cases, Nari in 2001 and Nakri in 2002, were chosen for study to explore the impact of assimilated GPS refractivity on model simulation. These two cases contain the maximum available soundings (four–five) for typhoons past Taiwan since the operation of both the CHAMP and SAC-C satellites. With the advent of COSMIC data, the number of available soundings will increase to about 30 in the outermost domain of a regional model near a specific initial time. Since GPS sounding is valuable due to retrieved moisture information, greater emphasis will be given to model performance for rainfall prediction associated with the typhoons. Numerical aspects, including model setups, will be introduced in section 2. The model results and performance assessments for the two selected cases will be presented in section 3. In this section, cycling 3DVAR is also conducted to explore the impact of complementary National Aeronautics and Space Administration (NASA) Quick Scatterometer (QuikSCAT) near-surface wind information on simulations of Typhoon Nari. Finally, conclusions are given in section 4.

2. Numerical aspects

a. MM5 3DVAR

The MM5 3DVAR method is based on minimization of a cost function defined as

$$J = \frac{1}{2}\{(\mathbf{x} - \mathbf{x}_b)^{\mathrm{T}}\mathbf{B}^{-1}(\mathbf{x} - \mathbf{x}_b) + [\mathbf{y}_{\mathrm{obs}} - \mathbf{h}(\mathbf{x})]^{\mathrm{T}}\mathbf{O}^{-1} [\mathbf{y}_{\mathrm{obs}} - \mathbf{h}(\mathbf{x})]\}, \quad (1)$$

where

$\mathbf{x}$, analysis variable vector (n-dimensional);
$\mathbf{x}_b$, background variable vector (n-dimensional);
$\mathbf{y}_{\mathrm{obs}}$, observation vector ($m$-dimensional);
$\mathbf{B}$, background error covariance matrix ($n \times n$);
$\mathbf{O}$, observation error covariance matrix ($m \times m$), and
$\mathbf{h}$, nonlinear operator to transform the analysis variable vector to the observation vector.

At the extreme, the derivative of J would vanish; that is,

$$\nabla J = 0 = \mathbf{B}^{-1}(\mathbf{x} - \mathbf{x}_b) - \mathbf{H}^{\mathrm{T}}\mathbf{O}^{-1}(\mathbf{y}_{\mathrm{obs}} - \mathbf{H}\mathbf{x}), \quad (2)$$

and the estimate of $\mathbf{x}$ can thus be obtained as

$$\mathbf{x}_a = \mathbf{x}_b + (\mathbf{B}^{-1} + \mathbf{H}^{\mathrm{T}}\mathbf{O}^{-1}\mathbf{H})^{-1}\mathbf{H}^{\mathrm{T}}\mathbf{O}^{-1}(\mathbf{y}_{\mathrm{obs}} - \mathbf{H}\mathbf{x}_b), \quad (3)$$

where $\mathbf{H} = \partial\mathbf{h}/\partial\mathbf{x}$ is the tangent linear approximation of the nonlinear operator $\mathbf{h}$. The transformation operation may be nonlinear and an incremental formulation based on the above linearity is used in MM5 3DVAR analysis to obtain the solution. The details of the minimization procedure for the solution may be found in Barker et al. (2003) and Vandenberghe and Kuo (1999).

The forward operator of local refractivity is related to pressure, temperature, moisture, and other existent compounds in the atmosphere. Bevis et al. (1994) investigated the relative errors associated with the constants in existent GPS radio refractivity formulas and gave a common form as

$$N = (n - 1) \times 10^6 = 77.6\frac{P}{T} + 3.73 \times 10^5\frac{P_w}{T^2}, \quad (4)$$

where n is the index of refractivity, P the atmospheric pressure, and P_w the water vapor pressure related to the specific humidity of the moisture. This forward operator simply dictates the relation of refractivity (N) to temperature (T) and moisture (q), the latter two as model variables that can be directly predicted by the model. The first term in (4) for dry-temperature effects is much larger than the second term for moisture effects. Since relative temperature changes in the troposphere normally are much smaller than relative moisture changes, the second term actually contributes to most of the refractivity increments. If any ancillary data (e.g., pressure or temperature) are available, then it can be used to solve (4) for the moisture. This equation is simple and its associated linear tangent and adjoint operators are much easier to implement as compared to ray-tracing operators (e.g., Zou et al. 1999). The GPS refractivity data are taken from the COSMIC Center at NCAR, which processes data observed by the CHAMP and SAC-C satellites. Currently, the GPS sounding profiles that can be retrieved by existing algorithms are down to 1-km height only.

The radio occultation observational covariance matrix used in the experiments is diagonal and thus all vertical correlations between the retrieved refractivity

measurements at different heights are ignored. This assumption is certainly not supportive of some existing dependence between observation data, but in the absence of statistical information on those correlations, the assumption ensures that the information content of the data is not underestimated. The diagonal elements (variances) are prescribed as a profile exponentially decreasing from 3°N at 100 hPa to 10°N at 1000 hPa. This error profile is based on the vertical exponential variation that is generally assumed for the actual atmospheric refractivity (Sokolovskiy 2001). The 3°N observational error value at the highest level accounts for 2°N error due to the antenna gain [measurement error; Sokolovskiy et al. (2001)] and 1°N for representativeness error. The 10°N observational error value near the surface is consistent with the 3% refractivity difference between CHAMP radio occultations and European Centre for Medium-Range Weather Forecasts (ECMWF) analyses found at 1000 hPa as reported by Kuo et al. (2004).

In the MM5 3DVAR approach, all observation errors are assumed to be uncorrelated in space and time so that the associated covariance matrix **O** is diagonal. The diagonal elements of the matrix **O** are prescribed as those used in the NCEP operational 3DVAR method (Parrish and Derber 1992). The background error covariance matrix **B** is prescribed as monthly mean forecast error variances derived from the yearly Penn State–NCAR MM5 forecast. The effect of spatial error correlations existing in **B** on the analysis vector then can be produced by a recursive filter (Lorenc 1992) with a correlation length of 10 model grid points. The background vector is given by previous forecast fields or first guesses from global model assimilation at the initial time. Hence, influences of conventional soundings and GPS occultation observations as well as model dynamics have been taken into account in the analysis.

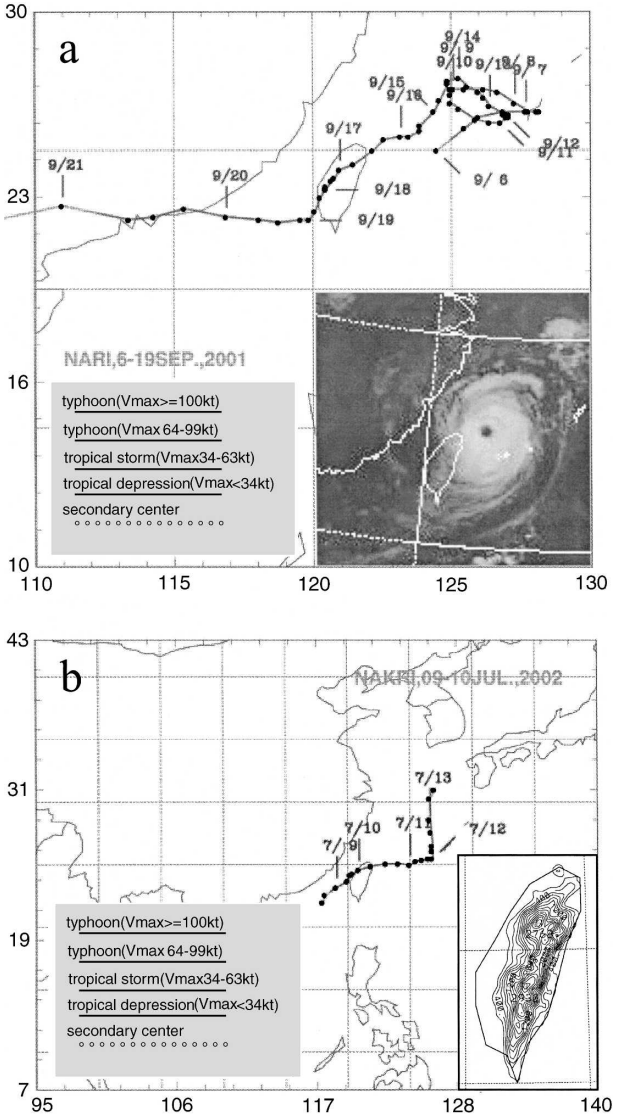

FIG. 1. The best tracks from CWB for (a) Typhoon Nari (Sep 2001) and (b) Typhoon Nakri (Jul 2002). The satellite image in (a) was observed at 0032 UTC 16 Sep 2001. Taiwan topography resolved in the third model domain (domain 3) is given in the lower-right corner of (b) with a contour interval of 200 m.

b. Simulation setups

Two recent cases were chosen for study: Typhoon Nari in September 2001 and Typhoon Nakri in July 2002. The best tracks of the two typhoons, provided by the Central Weather Bureau (CWB) in Taiwan, are shown in Fig. 1. Typhoon Nari with a southwestward track toward Taiwan is very unusual since such a track was observed only once in about 30 yr. On the contrary, Nakri exhibits a northeastward track; such northeastward tracks are less than one-fifth of the total tracks for typhoons past Taiwan. The two cases were associated with torrential rainfalls and had a great impact on the environment of the island.

The model simulations employ three nested domains at 45-, 15-, and 5-km resolutions, respectively. The initial first guess uses the NCEP Aviation Model (AVN) global analysis in the simulation for Nari and the European Centre (EC) Tropical Ocean Global Atmosphere (TOGA) global analysis for Nakri. As is well known, the influences of some satellite data have been incorporated into both global analyses. The conventional rawinsondes and surface observations used in the MM5 3DVAR simulations are taken from CWB. The integration time is 72 h for both cases using MM5 version 3.5 with explicit treatments (Goddard's scheme) for ice/graupel physics in all of the domains; Kuo's

TABLE 1. A list of the occultation refractivity observations from the CHAMP and SAC-C satellites used in the simulations for Typhoons Nari (2001) and Nakri (2002).

Cases	Satellite	Observation time	Occultation location	Point No.
Nari (16 Sep 2001)	CHAMP	0145 UTC	(51.50°N, 154.03°E)	1
	SAC_C	0222 UTC	(38.01°N, 140.00°E)	2
	SAC_C	0226 UTC	(25.04°N, 136.96°E)	3
	SAC_C	0230 UTC	(4.18°N, 136.57°E)	4
Nakri (7 Jul 2002)	CHAMP	1129 UTC	(22.29°N, 145.44°E)	1
	CHAMP	1132 UTC	(34.42°N, 142.60°E)	2
	CHAMP	1256 UTC	(5.83°N, 128.99°E)	3
	CHAMP	1259 UTC	(16.29°N, 108.57°E)	4
	CHAMP	1301 UTC	(22.73°N, 123.3°E)	5

scheme and Grell's scheme for cumulus parameterization in domain 1 (largest) and domain 2 (second largest), respectively; and the Blackadar scheme for PBL parameterization in all of the domains. Detailed descriptions of MM5 and its physical contents are given by Dudhia (1993).

The maximum height of the Central Mountain Range (CMR) in Taiwan resolved in domain 3 is about 3000 m, as shown in Fig. 1. In addition to the primary CMR, there is also the Shei-Shan Mountain Range (the northern mountain range, a northeastward extension of the CMR) and the isolated Dar-Tun Mountain at the northern tip of the island. Past observations indicated that the geometry of the mountains in Taiwan plays an important role in the distribution of rainfall associated with an invading typhoon. Hence, the 5-km horizontal resolution used in this study should be plausible for the purposes of this study with a focus on mesoscale weather evolution. Both cases will be simulated with or without GPS refractivity assimilated in the initialization. The GPS refractivity assimilation is performed by using the 3DVAR scheme for each mesh. Table 1 provides a list of the available occultation points for the two cases. We have reviewed the availability of all processed refractivity data from CHAMP and SAC-C for typhoons past Taiwan and found that the presented two cases contain the maximum GPS soundings in our assimilation time windows.

3. The results

a. The Nari case

Detailed discussions on simulations without GPS refractivity assimilation for Typhoon Nari were given by Huang et al. (2002). Prior to landfall, Nari was a moderate typhoon associated with a maximum gust wind of about 40 m s^{-1} as estimated from the satellite IR imagery (Fig. 1a) by CWB. Nari moved southwestward toward Taiwan, passed over the northern mountain range of Taiwan (Fig. 1a) and then migrated southward roughly along the west coast. Sensitivity tests on model initialization time indicate that the simulated Nari, when initialized at 0000 UTC 15 September, exhibits a slow southwestward displacement toward Taiwan in the first 2 days, but then recurves away from the island. As the initial time is set forward to 0000 UTC 16 September, the simulated typhoon then makes a landfall in the north-northeast of Taiwan. Based on several sensitivity tests on different bogussed vortices, simulations of the Nari typhoon are also sensitive to the initial vortex structure. In cases with a larger vortex size or stronger tangential wind, the cyclone moves farther away from Taiwan early in the simulation and does not make a landfall at all. To avoid the complexity of the interpretation due to the influence of vortex bogussing on the simulation and to isolate the impact of the GPS data, we thus made a decision not to adopt vortex bogussing in the present simulations.

The evolving features of the rainbands associated with Nari were clearly delineated by the reflectivity echoes from the radar observatory located near the northern tip of Taiwan (see Huang et al. 2002). According to the reflectivity echoes (not shown), Nari made a landfall in the north-northeast of Taiwan at 1340 UTC 16 September. As discussed in Huang et al. (2002), the organized spiral structures associated with the vortex seemed to deform gradually after landfall, but appeared to reintensify to some extent later as the vortex center moved slowly southward along the western slope base of the CMR (see Fig. 1a). Significant rainfalls, as shown in Fig. 2a, were produced mainly along the upwind slope of north Taiwan during the first stage when Nari was passing over the northern mountain range and the mountain at the northern tip of the island. Nari then moved along the west coast and continuously penetrated to central Taiwan with intensifying onshore flow. The later reintensification of Nari results in tremendous precipitation in the southwest of Taiwan (Fig. 2b). The observed 24-h accumulated rainfalls on

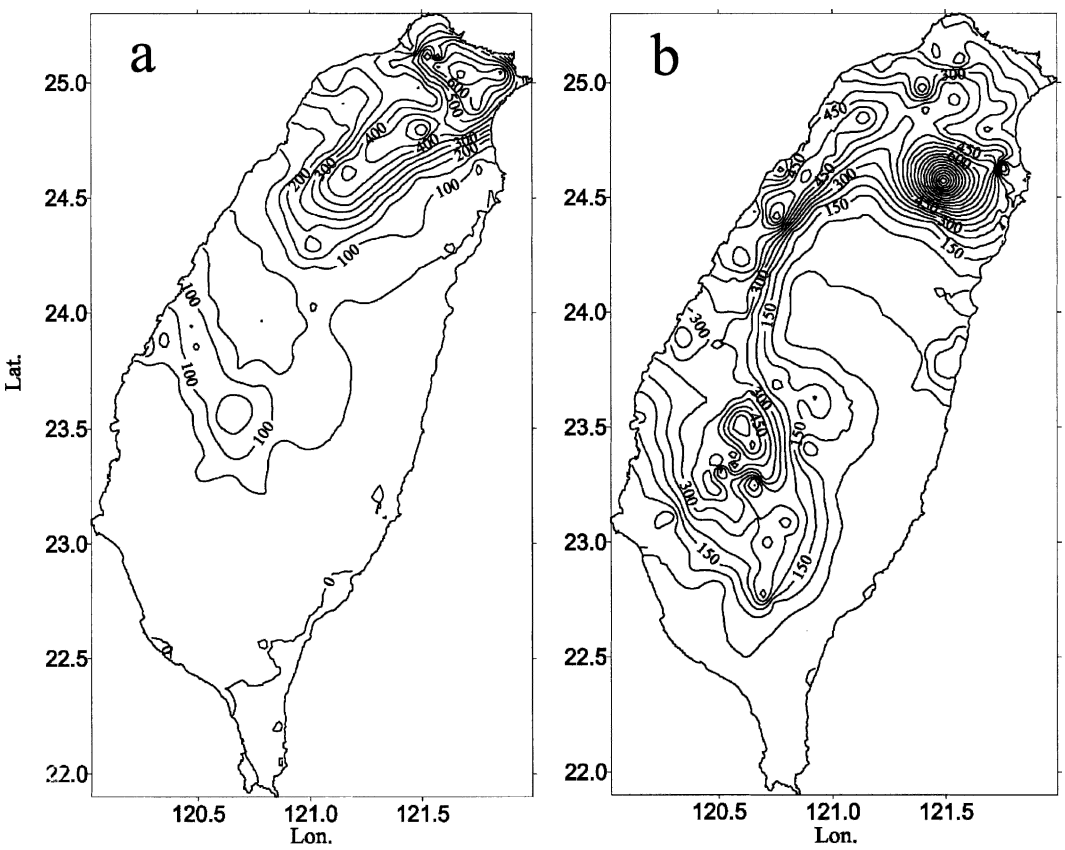

FIG. 2. The observed accumulated rainfall (mm) during (a) 0000–2400 UTC 16 Sep 2001 (711 mm) and (b) 0000–2400 UTC 17 Sep 2001 (1161 mm) for the Typhoon Nari case. The value in the parentheses indicates the amount of maximum rainfall. Contour intervals are 50 mm.

17 September have a maximum amount of 570 mm (at 23.5°N and 120.6°E) over the southwestern slope base of the CMR, while the maximum accumulated rainfall (with an amount of 1161 mm) during this event occurs on the northeastern slope.

Geometric distributions of occultation observations (figure not shown) from the CHAMP and SAC-C satellites exhibit 158 sounding points on 16 September 2001. Within a 3-h window of the model initial time (0000 UTC 16 September 2001), there are four occultation points within the largest model domain (see Fig. 3); their locations and observation times are listed in Table 1. The four retrieved refractivity profiles (not shown) available from the UCAR COSMIC Data Analysis and Archive Center (CDAAC) show an exponential increase in refractivity intensity with decreased height, which reflects the accumulated effects of the atmospheric air mass. At best, the retrieved refractivity profiles can only reach down to 2 km in height for this event. With the background information from the first guess (AVN global analysis), this data void at the lowest layer is not a problem for minimization in the 3DVAR simulations. Due to the dominance of the temperature in Eq. (4), the variations between the profiles of local refractivity at different occultation points seem quite small (not shown). Through the 3DVAR scheme, moisture increments corresponding to these small refractivity increments can be produced to a larger extent as will be shown later.

For the run with GPS refractivity assimilation (denoted as run GPS), the increments of computed local refractivity and temperature at $\sigma = 0.725$ are shown in Fig. 3. The local increments are defined as the differences between the initial fields with and without the GPS refractivity assimilation. All of the above increments are confined to circular zones at a radius of 500–600 km, which are typical responses of the 3DVAR modulation to individual observation soundings. The refractivity increments (Fig. 3a) show a maximum magnitude of about 10 units from occultation point 2 (near Japan), while the temperature increments (Fig. 3b) in general are less than 0.2°C. Since the local refractivity in the lower atmosphere usually is near 300 units, the refractivity increments of 10 units are only about 3% at

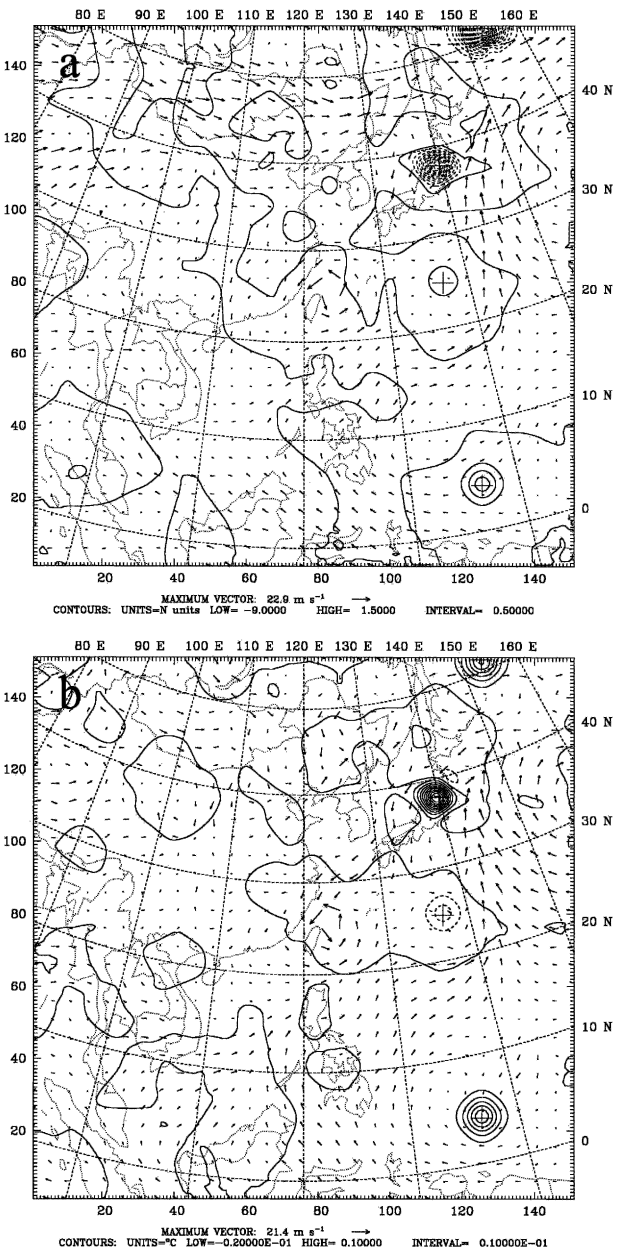

FIG. 3. The initial 3DVAR analyses in the GPS run for the Typhoon Nari case. (a) The refractivity increments (N units) and the wind vectors (m s^{-1}) at $\sigma = 0.725$ and (b) temperature increments (°C) at $\sigma = 0.725$ and the wind vectors (m s^{-1}) at $\sigma = 0.945$. The plus (+) sign indicates the occultation location. The increments are the differences between the initial conditions of the GPS run and the no-GPS run.

a maximum. Variations of the moisture increments near an occultation point are similar to corresponding refractivity increments in terms of distribution (not shown), with a maximum magnitude as large as 1.5 g kg^{-1}. The characteristic features of relatively larger recovery in moisture and relatively smaller recovery in temperature are consistent with the results of 4DVAR refractivity assimilation for a winter cyclone (Zou et al. 1995).

The vertical variations of the temperature and moisture increments over occultation points 2–4 (see Table 1) are examined herein; occultation point 1 is too close to the north boundary and thus is not plotted. The temperature increments for both the no-GPS and GPS runs are relatively smaller in all of the vertical profiles, due to the fact that the local refractivities are more sensitive to variations in moisture content. For point 2 (near Japan), most of the temperature increments are warming at the lower levels, whereas cooling exists at higher levels (e.g., above 6 km) but with smaller magnitudes (Fig. 4a). This low-level warming is associated with drying effects as large as 1.5 g kg^{-1} (Fig. 4b). At point 3

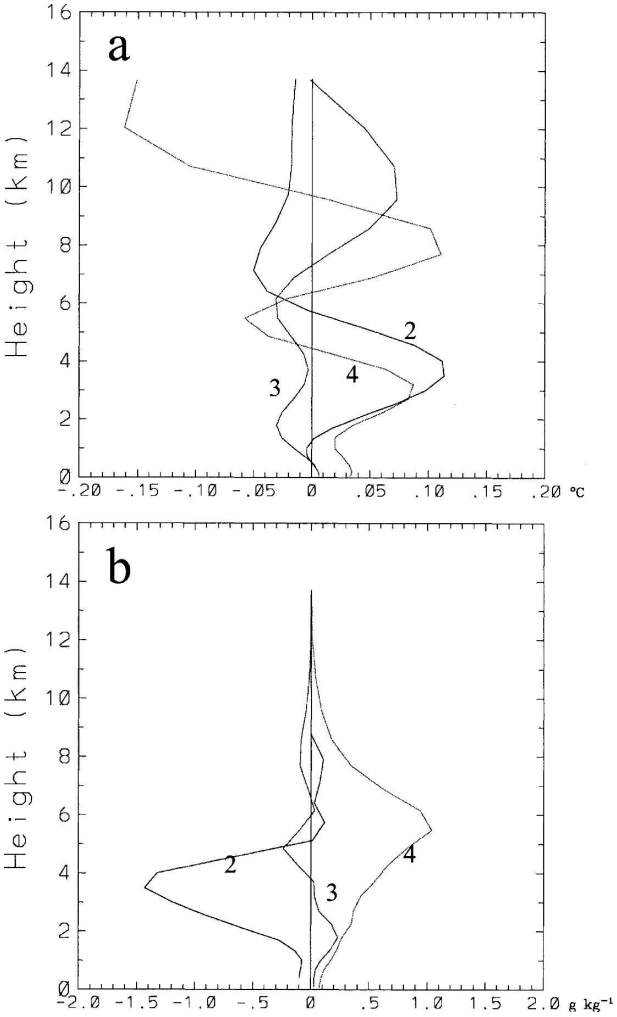

FIG. 4. The initial increments in (a) temperature (°C) and (b) moisture (g kg^{-1}) in the GPS run for Nari at the GPS occultation points 2–4, as indicated by the plus signs from upper to lower, respectively, in Fig. 3.

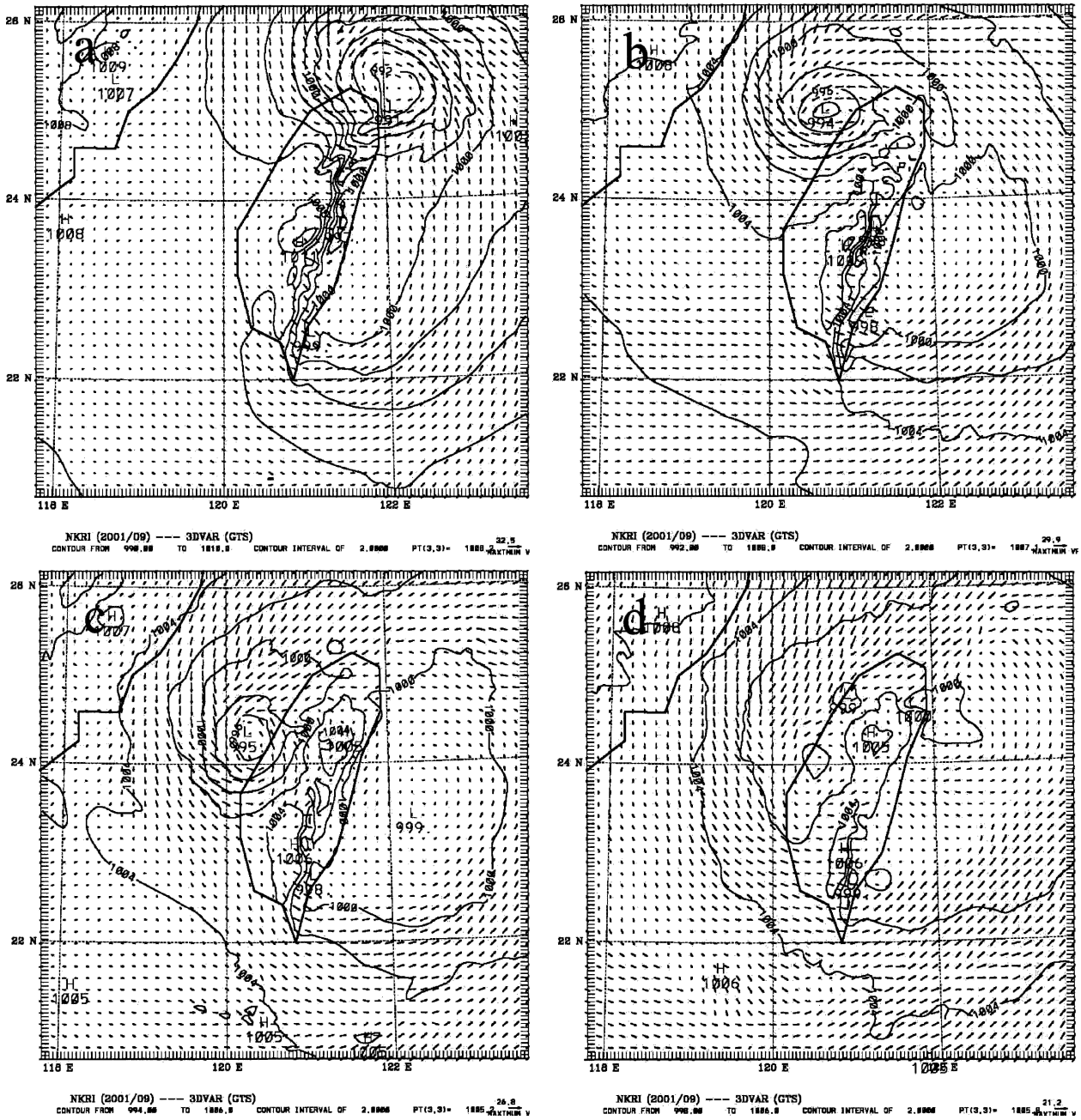

FIG. 5. The simulated sea level pressure (hPa) and near-surface horizontal wind (m s^{-1}) in domain 3 at (a) 12, (b) 24, (c) 36, and (d) 48 h in the no-GPS run for Nari.

east of Taiwan, however, there are cooling effects below 7 km (Fig. 4a) and moistening effects below 4 km. The moisture increments at point 4 east of the Philippines are positive throughout the troposphere at a maximum amount of about 1 g kg^{-1}, while the temperature increments are positive mainly in the lowest 4 km, above which they become somewhat erratic. Thus, both soundings from points 3 and 4 favor an adjustment of the initial guess to more wetness in the lower atmosphere, and such modifications help reconstruct the moister conditions over the ocean.

The simulated wind and pressure fields at the lowest level in the no-GPS run are shown in Fig. 5. In the no-GPS run, the central low after 12-h integration has strengthened to 991 hPa at 1200 UTC 16 September, with an intensifying upslope flow that passes over the

northern mountain range and the mountain at the northern tip. In response to the strong upslope flow, intense rainfall is produced mainly along the upwind slopes of these mountains during 0600–1200 UTC 16 September, as is evident in (Fig. 7a). As the vortex core moves to the northwestern coast by 0000 UTC 17 September, the upslope flow migrates southward (Fig. 5b) and passes over the northern slope of the CMR. The associated major rainfall also moves southward and extends roughly along the northwestern slope of the CMR (Fig. 7a). In fact, no intense rainfall is produced outside the intense vortex and at the lee sides of both the CMR and the northern mountain range, indicating that the mechanism that produces the intense rainfall may closely bear on the enhancement of the cyclonically rotating rainbands at confrontation with the steep topography, as discussed in Huang et al. (2002). The upslope flow over the north of the CMR has weakened significantly at 36 h as the vortex center moves farther southwestward (Fig. 5c). The simulated vortex center then keeps a slow southwestward movement roughly along the coast by 48 h. The vortex circulation at 48 h is associated with strong inland penetrating flow (Fig. 5d), which results in intense rainfall in the southwest of Taiwan (see Fig. 7b). It appears that the vortex's circulation regains some intensity during its alongshore movement, despite the fact that its core structure has deformed significantly. Thus, the observed torrential precipitation in the southwest of Taiwan can be attributed largely to the effect of the onshore flow convergence that may be enhanced by upstream blocking of the CMR. This feature may deserve further investigation on moisture flux budgets to understand why the vortex circulation with a deformed core structure may produce such an exceptionally large amount of rainfall over the plain coast.

Compared to the no-GPS run, the simulated vortex circulation (not shown) is similarly early in the simulation (e.g., at 12 h) in the GPS run and hence their earlier accumulated rainfalls remain similar (Figs. 7a,c). For the GPS run, the vortex center moves to a position near the northwest coast at 24 h and is endued with a southward track along the west coastline by 36 h (Fig. 6). As seen in Fig. 7, with a vortex track closer to the coast, the GPS run better captures the features associated with local maxima in accumulated rainfall over the southwestern and northeastern slopes of the CMR during 24–48 h, although not to a significant extent, as compared to the observations (Fig. 2).

The simulated tracks in both the no-GPS and GPS runs are shown in Fig. 8a; both the best tracks from CWB and the Joint Typhoon Warning Center (JTWC) are also plotted for comparison. The relatively coarser

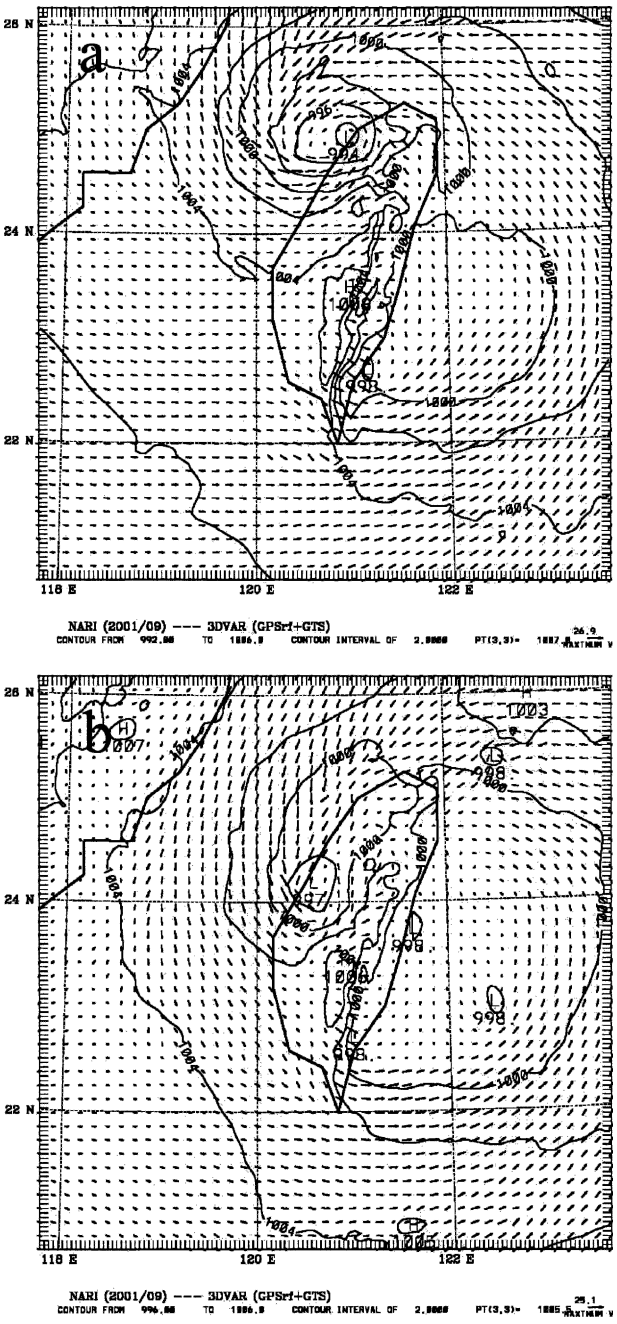

FIG. 6. The simulated sea level pressure (hPa) and near-surface horizontal wind (m s^{-1}) in domain 3 at (a) 24 and (b) 36 h in the GPS run for Nari.

resolution used by JTWC has led to a prediction that the track will travel east of the CMR. There are no noticeable deviations between the two tracks early in the simulation for the two runs. However, as can be seen, the track in the GPS run (denoted G) is closer to the west coast than in the no-GPS run (denoted N) later in the simulation, particularly after 24 h. Moreover, the

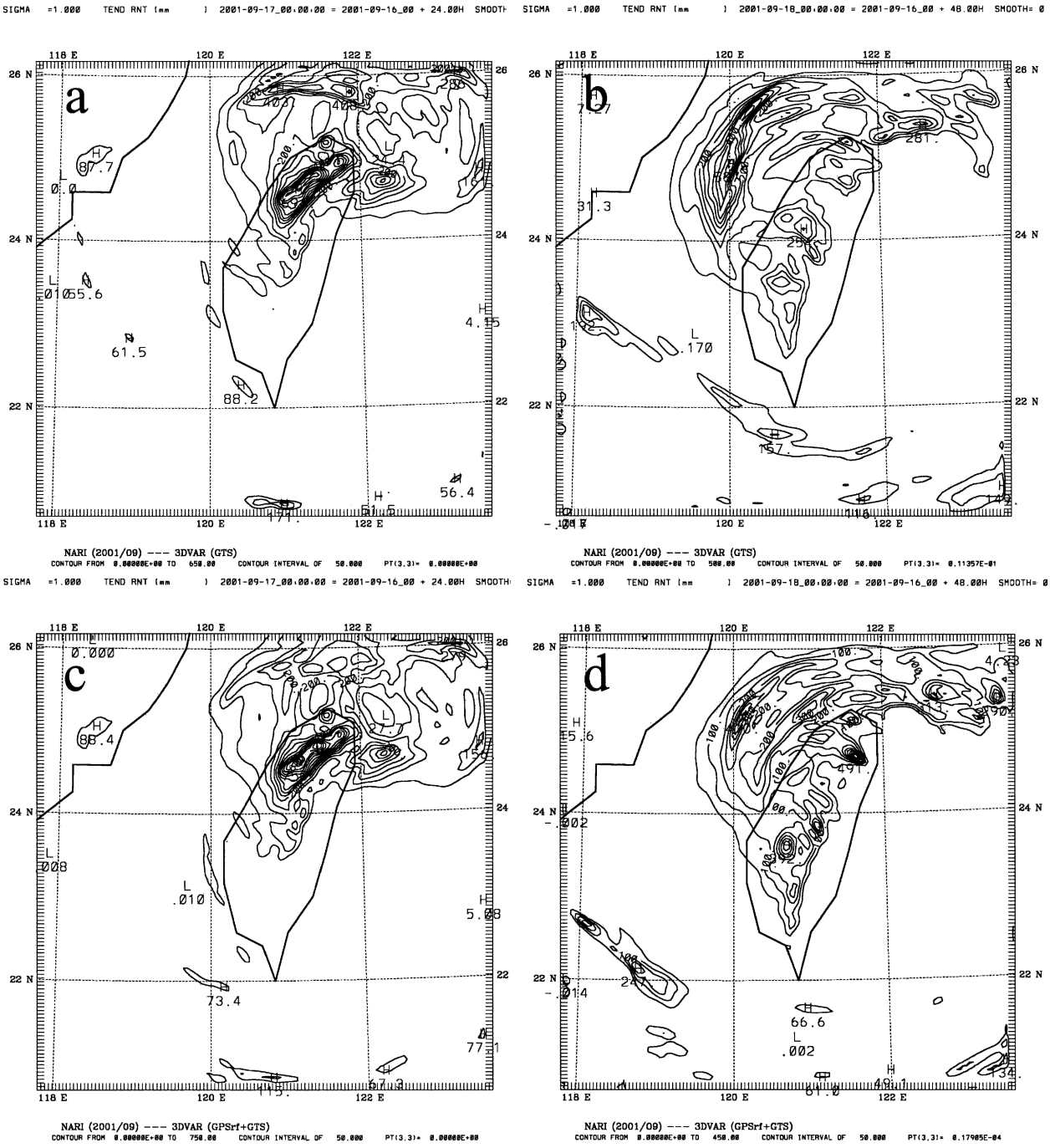

FIG. 7. The simulated accumulated rainfall in the no-GPS run during (a) 0000–2400 UTC 16 Sep 2001 and (b) 0000–2400 UTC 17 Sep 2001 for Nari, and (c), (d) as in (a), (b), respectively, but in the GPS run. Contour intervals are 50 mm in all panels.

vortex center at 48 h in the no-GPS run is still beyond 24°N, which is close to the position of the vortex at 36 h in the GPS run. At 48 h, the vortex in the GPS run has moved farther southward despite the fact that the center is not well distinguished (not shown). Hence, the track in the GPS run agrees better with the best track.

A sensitivity test of the GPS run without the GPS sounding at point 3 (east of Taiwan), denoted GPS-3, has been conducted to identify the role of the influence of this sounding in the simulation. Without this sounding, the track remains little changed early in the simulation, whereas the vortex considerably slows down at

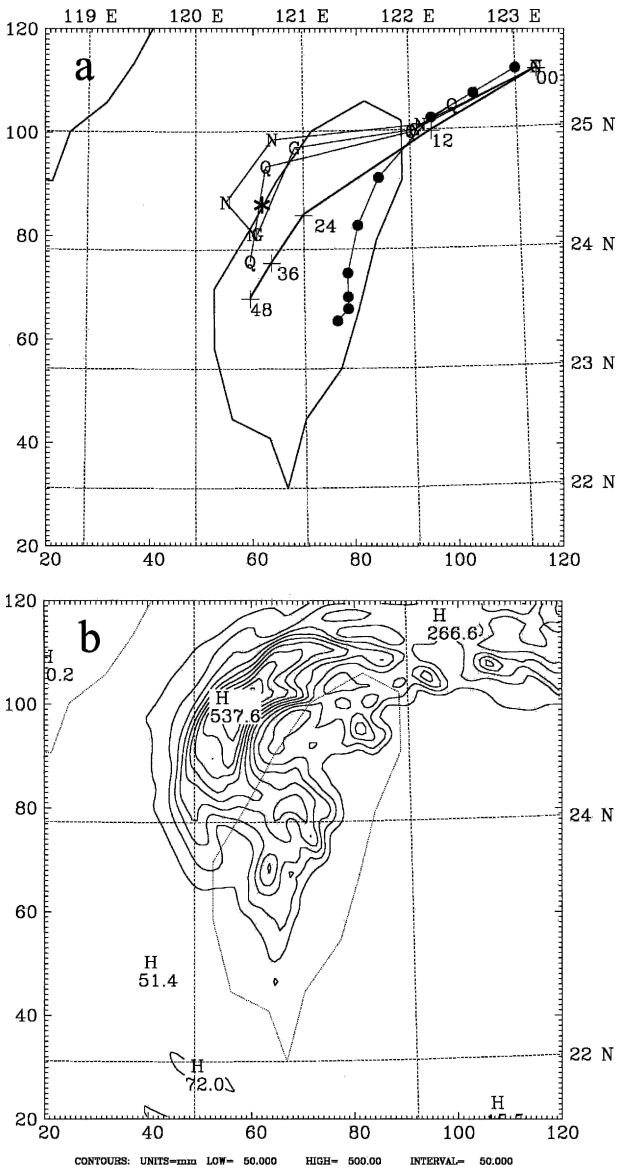

FIG. 8. (a) The simulated tracks for Nari every 12 h, marked by Ns, Gs, and Qs for the no-GPS run, the GPS run, and the Q-GPS run, respectively; the best track (bold line) from CWB is marked by plus signs. The best track from JTWC (marked by solid circles) at an interval of 6 h is also plotted. The asterisk indicates the position of the vortex center at 36 h in the GPS-3 run. (b) The accumulated rainfall during 24–48 h (with a contour interval of 50 mm) in the GPS-3 run.

later times, for example, at 36 h (see the asterisk in Fig. 8a) as it moves to the west coast. Due to the slowdown of the vortex, the attendant accumulated 24-h rainfall on the second day is less intense as is evident in Fig. 8b. The two rainfall maxima confined to the northeastern and southwestern regions of Taiwan are not as prominent as in the GPS run. Thus, the sounding at occultation point 3 has played a role in the improvement of the simulation.

The differences between the simulated results with and without GPS refractivity assimilation indicate a positive impact of the refractivity data on model prediction. Objective evaluations on accumulated rainfall given in a later section further indicate that the positive impact is statistically meaningful for intense rainfall prediction. To understand how the influences of the sounding information are spread throughout during the simulation, differences in circulation evolutions between both the GPS and no-GPS runs need to be investigated. We probe the differences in the predicted temperatures and moistures in both simulations. There are salient differences in temperature near the occultation points at 12 h with a maximum magnitude now increased to 1.4°C (not shown), resulting from their initial differences at the sounding points. The temperature differences from the two southern soundings then become more dispersive at later times (e.g., 24 and 36 h) as is evident in Fig. 9. At 36 h, the differences at lower levels, due to the sounding east of Taiwan, become widespread over the ocean and circulate around the outer typhoon vortex. Now, the differences in temperature (cooling or heating) can be as large as 2°C by this time. Since the differences from occultation point 4 are still farther southeast of the domain and are not contiguous to these increments in the vicinity of Taiwan, the typhoon simulation should be more impacted by occultation point 3. This may explain why the track and rainfall predictions in the GPS-3 run are not improved as much as in the GPS run.

The corresponding moisture increments at 12 h (not shown) exhibit two major modification zones at most of the levels, one with negative values near Japan and the other with positive values southeast of Philippine in response to their initial increments (Fig. 4b). The northern one advects northeastward with the large-scale flow and its intensity gradually dissipates with time. At 24 h, most of the moisture increments, with a maximum magnitude of 2 g kg^{-1}, are produced east and southwest of Taiwan, and these features are most likely related to the temperature differences that existed there earlier. Similar to the spreading of temperature increments, most of the moisture increments are confined within the typhoon circulation, with some exceptions southeast of the Philippines that result from propagation of the existent differences at previous times. At lower levels (e.g., $\sigma = 0.91$), a salient feature with large positive moisture increments (up to about 2.8 g kg^{-1}) is present east and southeast of Taiwan at 36 h (Fig. 10a), which may be responsible for the improvement of intense rainfall prediction. This positive moisture increment is

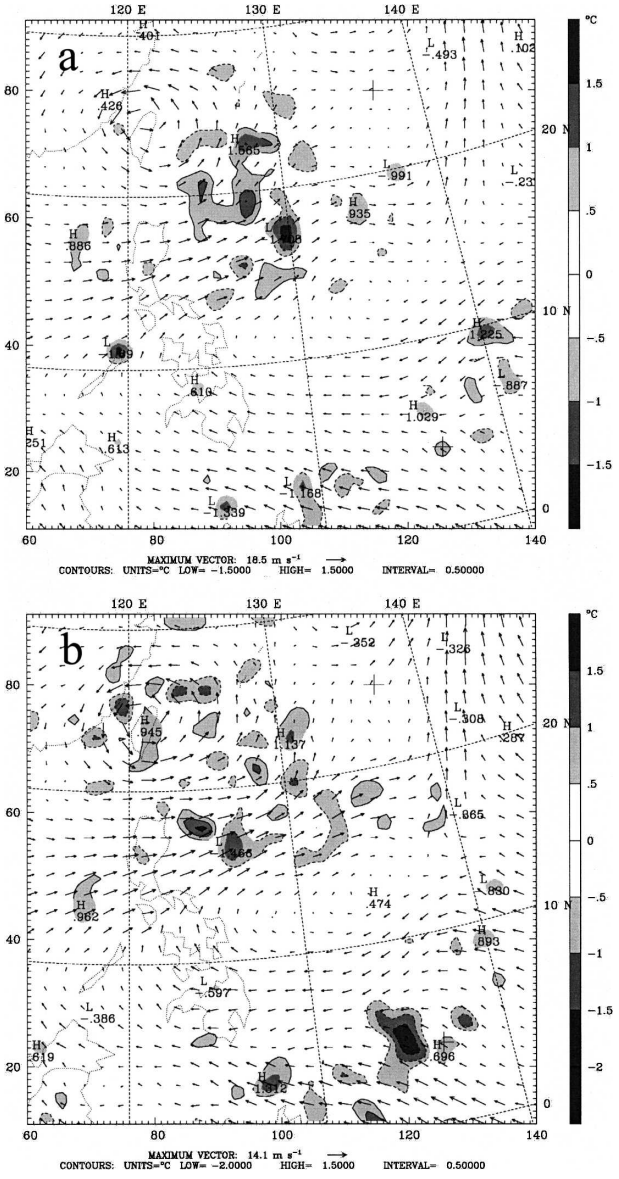

FIG. 9. The differences between the simulated temperatures (°C) at $\sigma = 0.625$ at (a) 24 and (b) 36 h in the GPS run and the no-GPS run for Nari. The wind field (m s^{-1}) is also overlapped. Shown in (a) and (b) is only a portion of domain 1 and zero contours are not plotted.

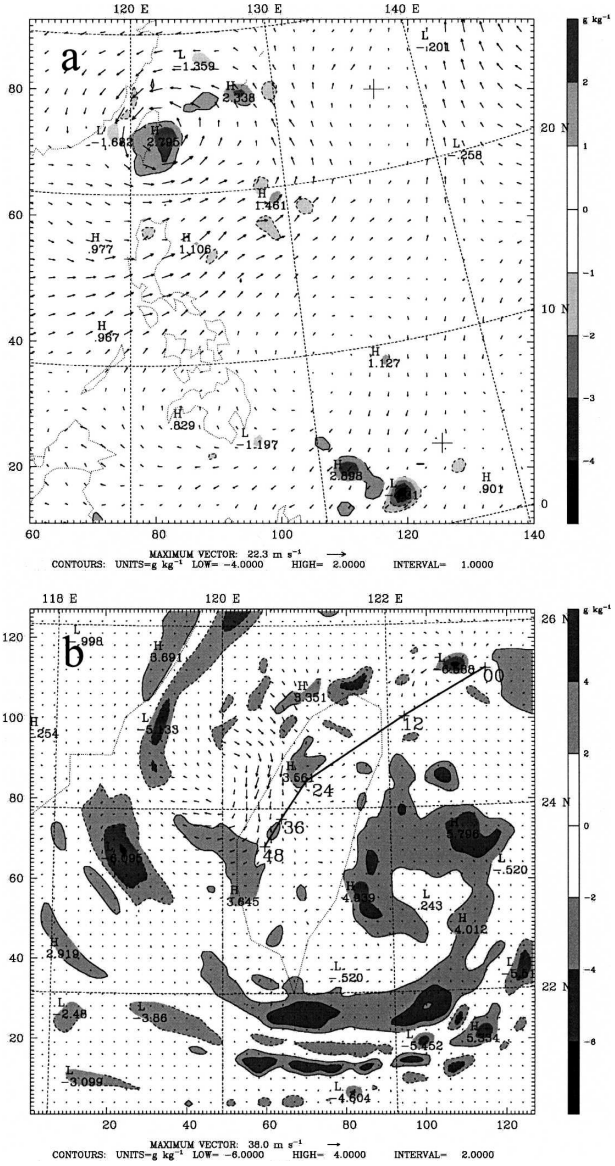

FIG. 10. (a) The differences between the simulated moistures (g kg^{-1}) at $\sigma = 0.910$ at 36 h in domain 1 in the GPS run and the no-GPS run for Nari with the wind field at the same level overlapped; (b) as in (a) but in domain 3 with the wind increments overlapped. The best track is also plotted as in Fig. 8. Zero contours are not plotted.

associated with smaller wet refractivity but higher temperature (not shown). The differences between the simulated moistures in domain 3 at 36 h in the GPS run and no-GPS run show large moistening effects (up to about 6 g kg^{-1}) in the regions of the spiral rainbands just east of Taiwan and smaller effects on the west coast (Fig. 10b). These additional moistening effects will be favorable for more intense rainfall. Consequently, the major differences in the horizontal wind are primarily southward near the midwest coast, which might play a role in the farther southward track in the GPS run than in the no-GPS run. These analyses indicate that the results later in the simulation are sensitive to small initial increments and thus the observations over data-sparse regions may play a role in the structural evolution of the typhoon. As a result, the predictability of accumulated rainfall is improved as the evolution of the system gradually benefits from the initial increments. In the following simulations for Typhoon Nakri, similar

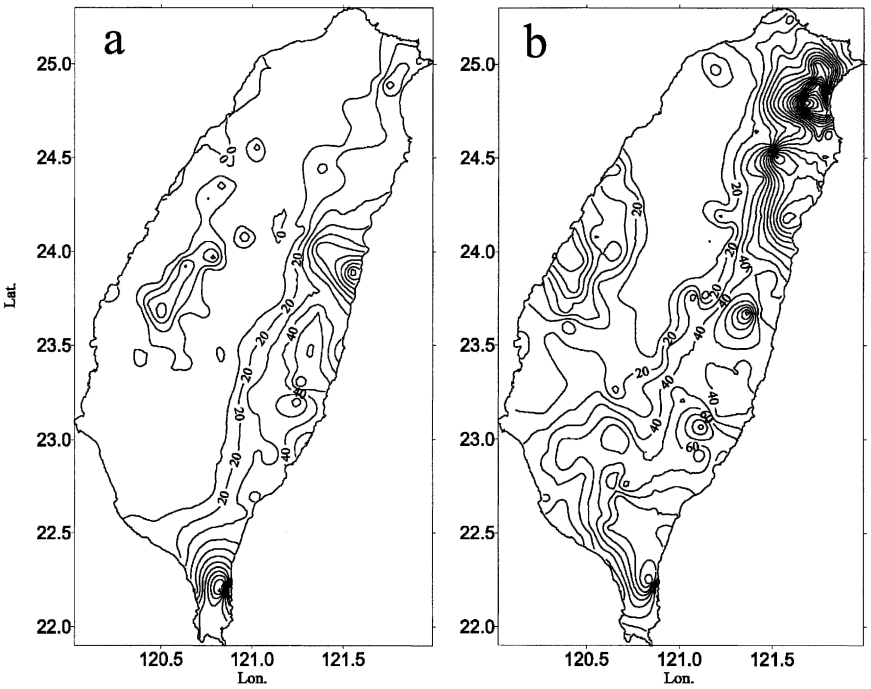

FIG. 11. The observed accumulated rainfall during (a) 1200 UTC 7 Jul–1200 UTC 8 Jul 2002 (122 mm) and (b) 1200 UTC 8 Jul–1200 UTC 9 Jul 2002 (207 mm) for the Typhoon Nakri. The value in the parentheses indicates the amount of maximum rainfall. Contour intervals are 10 mm.

improvement on accumulated rainfall prediction is also found.

b. The Nakri case

The Nakri storm system took a track past Taiwan from the southwest and was categorized as a tropical cyclone on 9 July 2002 (Fig. 1b). The radar reflectivity echoes at 3-h intervals indicate that Nakri produced vigorous localized convection but did not possess well-defined spiral rainbands (figure not shown). Most rainfalls during the simulation period are present to the east of Taiwan, with maxima at the southern tip (122 mm) on the first day and near the northeastern corner of the island (207 mm) on the second day as is evident in Fig. 11.

The model initial time for Nakri was set to 1200 UTC 7 July 2002. Within 3 h of the initial time, five GPS occultations took place in the largest model domain (see Table 1), as indicated in Fig. 12. All the GPS occultation points are located near the coast or over the ocean, one just southeast of Taiwan within the east flank of the Nakri circulation (Fig. 12a). For this case, the retrieved refractivity (not shown) can also reach only 2-km height at best. The differences in model local refractivity after GPS refractivity assimilation are less than 10 units in the midtroposphere (not shown), and the temperature increments remain less than 0.2°C (not shown). These results are consistent with the initial increments from the soundings in the Nari case. The initial moisture increments up to 1.4 g kg^{-1} are also confined near the occultation points in this case as can be clearly seen in Fig. 12a.

The vertical distributions of the moisture increments at occultation points 2–5 are shown in Fig. 12b. Of particular interest is occultation point 5, just southeast of Taiwan, which shows positive moisture increments up to 1 g kg^{-1} above 3 km. The effects from point 4 (in the southwest of the domain) produce positive moisture increments throughout the domain depth, with a maximum amount of 1.5 g kg^{-1} near 4 km. Contributions are more negligible from point 3 and are essentially negative from point 2 (east of Japan). Hence, both points 4 and 5 might be expected to have greater impacts on the simulation of Nakri. Again, the temperature increments are less significant and have relatively smaller magnitudes of only 0.2°C in the troposphere (not shown). These characteristics of the moisture and temperature increments for Nakri appear to be in accordance with the results for Nari. Hence, we may conclude that modi-

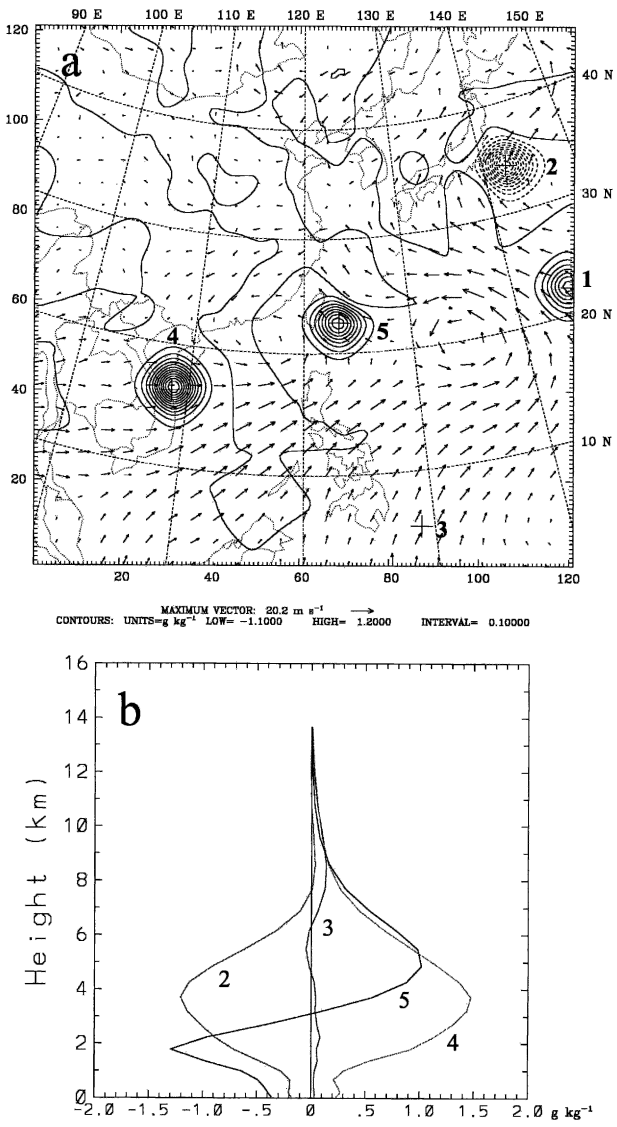

FIG. 12. The initial 3DVAR analyses for Nakri. (a) The moisture increments (g kg^{-1}) at $\sigma = 0.525$ and the wind field (m s^{-1}) at $\sigma = 0.945$; (b) the vertical profiles of moisture increments (g kg^{-1}) at the GPS occultation points 2–5 (marked by the plus sign).

fications from the GPS occultation soundings are essentially confined to a localized zone with much greater adjustments for moisture.

The simulated wind and pressure fields at the lowest level at 24 and 48 h in the no-GPS run and the GPS run are presented in Fig. 13. East of Taiwan, southeasterly flow is a salient feature early in the simulation (not shown) and the east slope is more or less associated with upslope flow. To the west of Taiwan, the sheltering effects result in a weak wake zone with most of the southwestward flow along the coast throughout the simulation (Figs. 13a,b). The inclusion of GPS refractivity in the simulation does not produce prominent differences early in the simulation (Fig. 13c). However, the southwestward flow, just south and southeast of Taiwan, appears to be stronger at 36 h (not shown) and the low to the southeast of Taiwan is more discernible and indeed is stronger at 48 h (Fig. 13d) in the GPS run. Since all of the model physics and numerical schemes are the same for both the no-GPS and GPS runs, the results indicate the sensitivity of model simulation to small discrepancies in the initial conditions.

The simulated accumulated rainfalls in the first day for both the no-GPS and GPS runs in general have similar geometric distributions as is seen in Fig. 14, and both are significantly larger than the observations. On the second day of the GPS run, the pronounced low, just southeast of Taiwan, produces larger accumulated rainfall (195 mm) to the northeast of Taiwan, which is much closer to the observed in terms of magnitude and position. Also, in the no-GPS run, the 24-h accumulated rainfall (Fig. 11b) along the mideast slope of the CMR appears to be considerably larger than the observed. For this case, both runs capture very well the features of the rain shadow region to the west of Taiwan and the major rainfall along the east slope of the CMR; despite that, however, some discrepancies in rainfall distributions remain evident.

The improvement in the GPS run may possibly be a benefit of the GPS sounding at point 4, which is upstream, southwest of Taiwan (see Fig. 12a). To probe this possibility, we also conducted a sensitivity test of the GPS run with the removal of point 4 (denoted GPS-4). The accumulated rainfall in the first day in this GPS-4 run in general is similar to that in the GPS run, except to the southeast of Taiwan with relative deficits (figures not shown). In the GPS run, the influence of the initial moisture increments from point 4 has propagated to the southeast of Taiwan by 12 h, due to the westerly to southwesterly flow south and southwest of Taiwan. The GPS-4 run then gradually differsfrom the GPS run in accumulated rainfall after 24 h. Although the initial conditions for the GPS-4 run are relatively short of moisture near point 4, the simulated results show considerably larger accumulated rainfall maxima in the northeast of Taiwan (328 mm) and slightly offshore east-southeast of Taiwan (307 mm) on the second day, as seen in Fig. 15. The relative wind (between the GPS-4 and GPS runs) near the surface at 48 h shows noticeable inland, upslope components near northeast Taiwan and more convergent flow offshore southeast of Taiwan, which appears to be in coherence with the presence of the two larger rainfall maximums on the second day in the simulation. Thus, the major accumu-

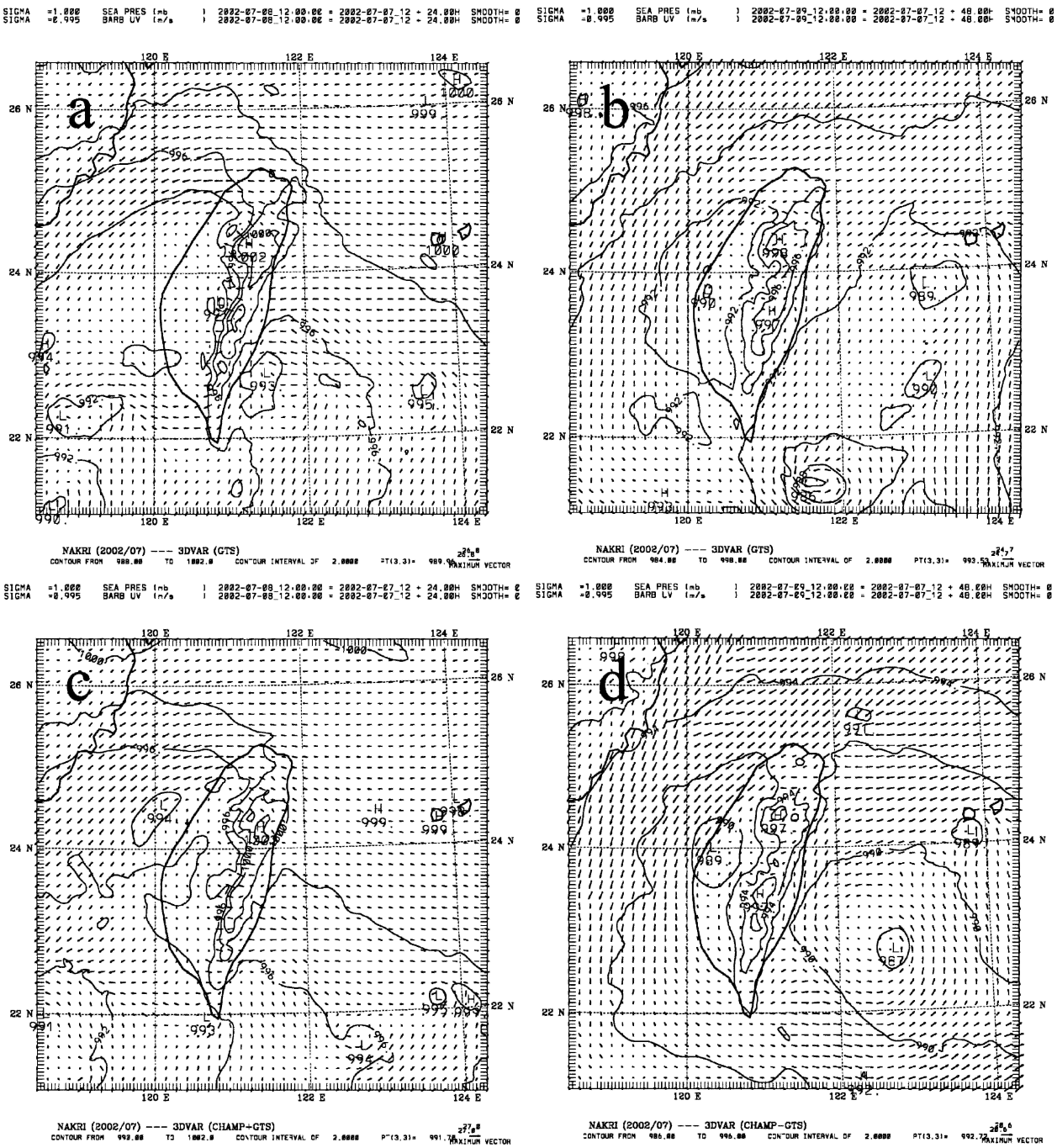

FIG. 13. The simulated sea level pressure (hPa) and near-surface horizontal wind ($m\ s^{-1}$) in domain 3 for Nakri at (a) 24 and (b) 48 h in the no-GPS run. (c), (d) As in (a), (b), respectively, but for the GPS run.

lated rainfalls on the second day in the GPS-4 run are overpredicted, as compared to observations in Fig. 11b. The above salient discrepancies in rainfall prediction stem only from removal of one upstream sounding. This sensitivity test also elucidates the predictability of intense rainfall for a typhoon past a steep mountain.

c. Impact assessments of GPS data

The above overall comparisons for the two cases (Nari and Nakri) are supportive of a positive impact of GPS refractivity assimilation on model prediction. To give a fairer judgment on the model performances with and without GPS refractivity assimilation, objective

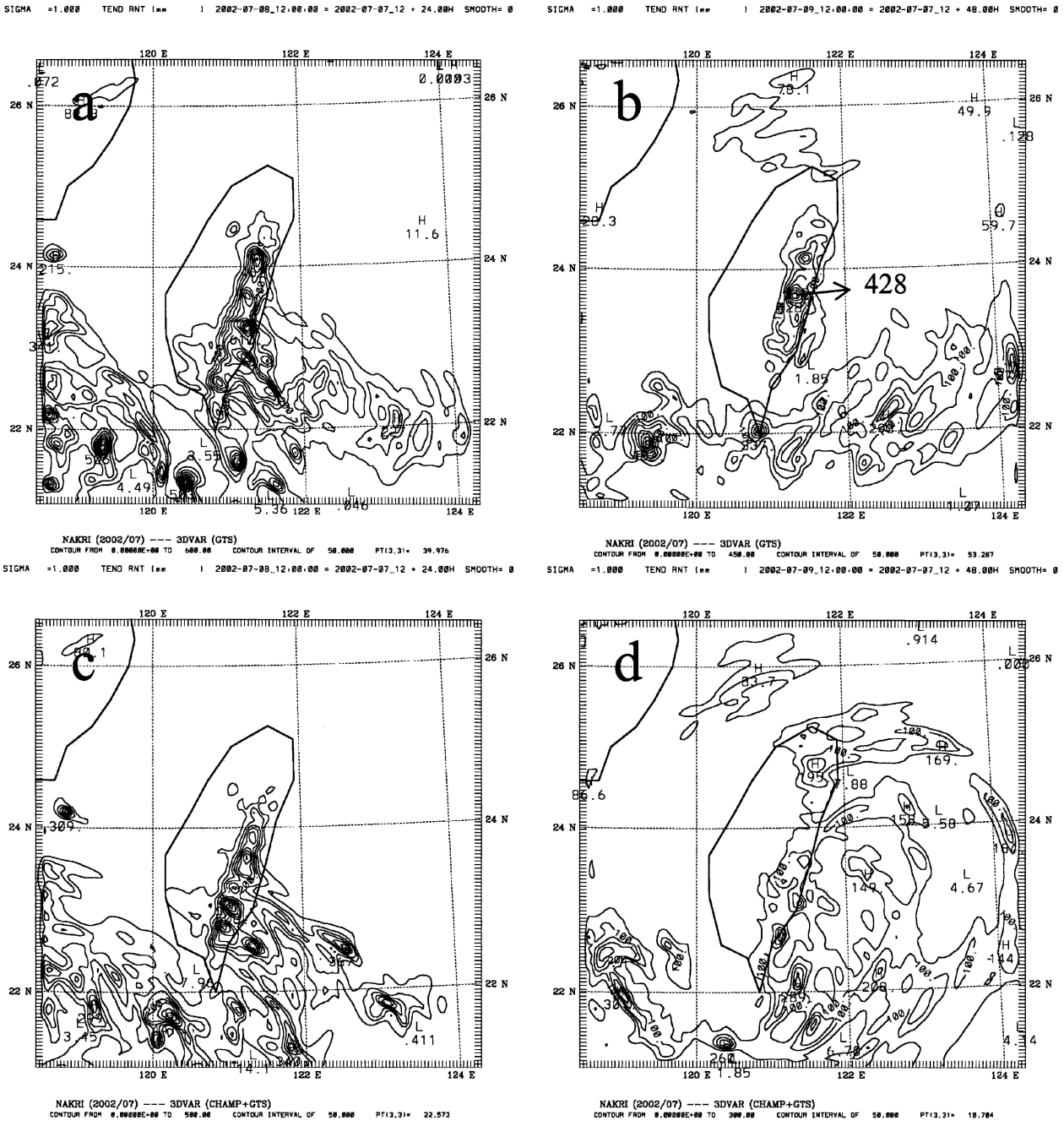

FIG. 14. The simulated accumulated rainfall in domain 3 in the no-GPS run during (a) 1200 UTC 7 Jul–1200 UTC 8 Jul 2002 and (b) 1200 UTC 8 Jul–1200 UTC 9 Jul 2002 for Nakri. (c), (d) As in (a), (b), respectively, but for the GPS run. Contour intervals are 50 mm in all panels.

evaluation was used to verify the predictions on accumulated rainfall against the observations. There are 362 rain gauge stations in Taiwan, most of which are located on the western plains and gentle slopes of the island. These data are interpolated into the 5-km resolution grids of the finest model mesh by the Cressman scheme, which employs an influential weighting radius of 10 km. There are about 1500 verification grid points on the island. The commonly used threat score is chosen to assess the accuracy of prediction on simulated accumulated rainfalls for both cases. Root-mean-square (rms) errors between the model results and objectively analyzed observations on the island are also computed. The threat score (TS) is defined as

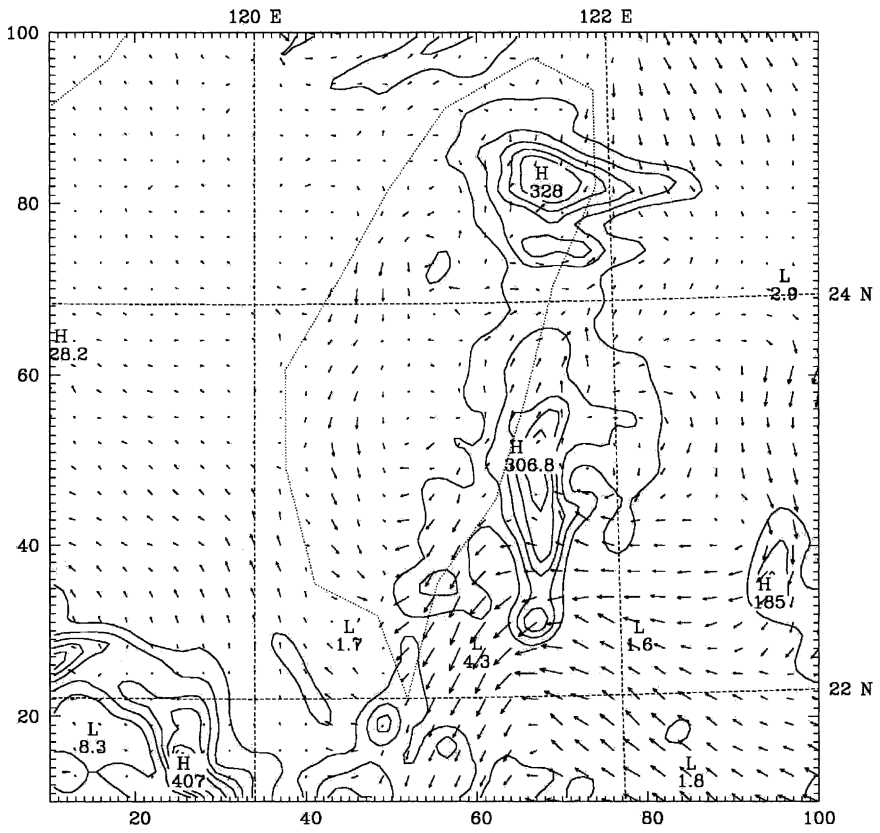

FIG. 15. The simulated accumulated rainfall (with a contour interval of 50 mm) in domain 3 in the GPS-4 run during 1200 UTC 8 Jul–1200 UTC 9 Jul 2002 for Nakri. The relative wind (the difference between the wind fields of the GPS-4 run and the GPS run) at $\sigma = 0.985$ at 48 h is overlapped.

$$\mathrm{TS} = \frac{A}{F + O - A}, \tag{5}$$

where A is the number of the grids on which both the forecast and the observation exceed the threshold, F is the number of the grids on which the forecast exceeds the threshold, and O is the number of the grids on which the observation exceeds the threshold.

Table 1 gives a statistical report of TS with thresholds of 0.25, 0.5, 1, 2, 5, 10, 15, 20, 25, 50, and 100 mm and rms errors for the 0–24- and 24–48-h accumulated rainfalls in the Nari and Nakri simulations with and without GPS refractivity assimilation. For typhoon simulations, evaluation on the 24-h accumulated rainfall is more relevant, because a small track error may produce large differences in the geometric patterns of rainfall intensity. Table 1 shows that TS is higher for smaller thresholds and gradually decreases with increased thresholds as expected. Use of a larger objective radius in the analysis also results in an increase in TS (up to 0.8 for small thresholds), which indicates the obvious fact that rainfall is typically island-wide for typhoon events. For the first day of the Nari case, the TS for the GPS run is about equal to or slightly worse than that for the no-GPS run. For the GPS run, however, there are dramatic increases in TS for the second day with larger thresholds, for example, from 0.462 to 0.504 for 50 mm and from 0.277 to 0.393 for 100 mm. The large increases in TS are also found for larger thresholds (e.g., 15, 25, 50, and 100 mm) in the GPS run of the Nakri case. In general, the prediction on larger rainfalls degrades significantly for Nakri with a considerably lower TS.

From Table 2, it is clear that the rms errors appear to be large for both the Nari and Nakri simulations. This result is quite plausible for rainfall prediction of typhoons past steep terrain since both magnitude and location of intense rainfall associated with the typhoon need to be well predicted by the model. Although the TS has a reasonable value of 0.5 for the second day of the Nari case, the associated rms errors have a magnitude of about 100 mm in spite of the fact that the observed maximum reaches 1161 mm as shown in Fig. 2b.

TABLE 2. Threat scores (TS) and root-mean-square errors (rmse's) (mm) of the accumulated rainfalls between 0–24 and 24–48 h for different thresholds for the Nari (2001) and Nakri (2002) simulations with difference sets of observation data included (GTS, only GTS at 0000 UTC; GPSrf, with extra GPS refractivity at 0000 UTC; QSCAT, with extra QuikSCAT near-surface wind at 0800–0900 UTC.

Cases	Nari GTS	NariGPSrf	Nari QSCAT	Nari GTS	Nari GPSrf	Nari QSCAT	Nakri GTS	Nakri GPSrf	Nakri GTS	Nakri GPSrf
Thresholds	0–24 h	0–24 h	0–24 h	24–48 h	24–48 h	24–48 h	0–24 h	0–24 h	24–48 h	24–48 h
0.25 mm	0.545	0.540	0.526	0.539	0.536	0.542	0.504	0.480	0.505	0.475
0.5 mm	0.544	0.539	0.520	0.538	0.535	0.544	0.482	0.464	0.498	0.448
1 mm	0.544	0.542	0.525	0.532	0.533	0.544	0.411	0.425	0.486	0.411
2 mm	0.530	0.524	0.521	0.527	0.531	0.542	0.376	0.363	0.463	0.378
5 mm	0.489	0.484	0.524	0.530	0.528	0.537	0.273	0.244	0.321	0.320
10 mm	0.489	0.492	0.542	0.527	0.530	0.538	0.182	0.174	0.277	0.278
15 mm	0.503	0.496	0.547	0.526	0.538	0.552	0.149	0.140	0.248	0.258
25 mm	0.524	0.496	0.525	0.543	0.531	0.552	0.126	0.127	0.233	0.235
50 mm	0.497	0.485	0.452	0.462	0.504	0.531	0.086	0.088	0.113	0.166
100 mm	0.473	0.444	0.404	0.277	0.393	0.462	0.009	0.000	0.000	0.129
Rmse (mm)	69.74	71.43	74.66	97.84	93.98	91.31	90.28	66.55	50.85	37.06

The simulated vortex for Nakri is considerably weaker than for Nari and hence its rms errors in general are smaller, in particular, for the second day. The rms errors for the second day are also smaller for the GPS run of both Nari and Nakri, which is consistent with their higher TS for accumulated rainfalls with larger thresholds.

We have shown before that the improved initial conditions with several realistic soundings do play a role in the evolution of typhoon circulation. The improved TS performances for both cases (Nari and Nakri) with GPS refractivity assimilation indicate that these data do have a positive impact on prediction of accumulated rainfall. For larger accumulated rainfall at the later stage, the improvement in the prediction, due to GPS data ingestion, is statistically more meaningful. Such noticeable improvement can be largely attributed to the improved track and vortex structure later in the simulation as the evolving typhoon has responded more positively to the accumulated changes from the initial increments.

d. Cycling 3DVAR with QuikSCAT wind

GPS occultation observations have a weakness in that no wind information can be directly retrieved. However, the wind field plays a more dominant role in geostrophic adjustment of a cyclone at low latitudes. The initial vortex resolved in the two case simulations is much weaker than that for the real typhoon. For example, the simulated low center for Nari only reaches 991 hPa after 12-h integration as shown in Fig. 6a, which is still considerably weaker than the observed (970 hPa). Such initial deviations from reality will adversely affect the vortex evolution in the simulation. Use of an initial bogus vortex for the typhoon may be helpful for improving the simulation. However, we have found that the simulated tracks with different bogussed vortices for Nari show even larger deviations from observations than the simulations without vortex bogussing.

The 3DVAR modulation principally produces very small, rather localized increments from the ingestion of a few presumed "observations" or first guesses, as found in previous numerical experiments (Huang et al. 2002). Wind information in a wider region may help 3DVAR to construct the vortex circulation in the first guess. This study focuses on the observed near-surface wind to be ingested at a specific prediction time for reinitialization by 3DVAR, namely, cycling 3DVAR. The near-surface wind observations are taken from the QuikSCAT satellite. During 0800–0900 UTC 16 September 2001, the satellite measurements cover the Nari's path. Hence, 0800 UTC 16 September 2001 is chosen as the reinitialization time (i.e., 8 h after the original initialization time). Within 2 h of the reinitialization time, one GPS refractivity sounding at 30.89°N and 89°E also took place within the largest model domain. In this specific cycling experiment (denoted G-GPS), both the near-surface wind information and the GPS refractivity profile are ingested into a 3DVAR reinitialization that takes the model prediction at 0800 UTC as the first guess.

The QuikSCAT wind observations near the surface during 0800–0900 UTC 16 September 2001 are shown in Fig. 16. The observed oceanic wind field displays a clear picture of the environmental flow embedded within a cyclonic vortex just northeast of Taiwan. The observations from the QuikSCAT instrument are consistent with the global analysis on 0000 UTC 16 September 2001, despite that the retrieved maximum wind speed is only about 24 m s^{-1} in the interior of the cy-

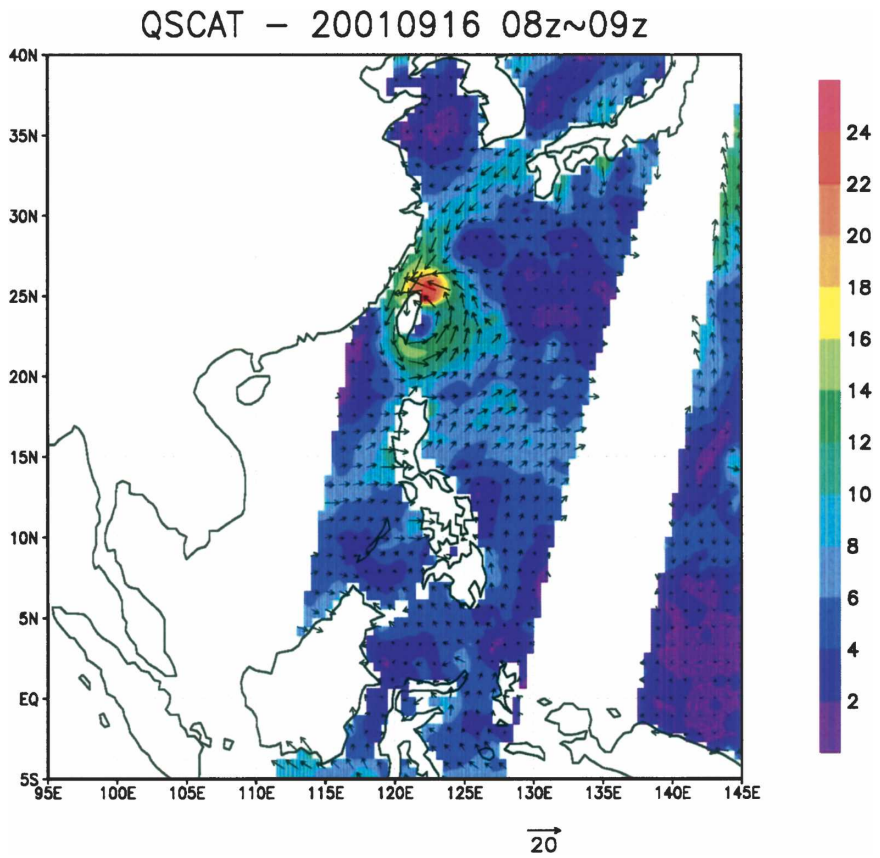

FIG. 16. The observed QuikSCAT near-surface wind (m s^{-1}, reference vector at bottom) during 0800–0090 UTC 16 Sep 2001, with the right (left) swath observed at 0800 (0900) UTC. Colored contours are for wind speeds.

clone. Figure 17 shows the initial increments of wind and moisture at $\sigma = 0.870$, in response to the observations including both the wind and GPS sounding. The moisture increments from the GPS sounding increase with height, from 0.54 g kg^{-1} at the surface to a maximum of 1.4 g kg^{-1} at $\sigma = 0.870$. The wind increments do exist only in the nearby region of an observation point, with a magnitude of about 6 m s^{-1} in the lower 2–3 km, above which the intensity gradually decreases with height. The wind vectors near east Taiwan are primarily northeasterly, which may facilitate a southwestward movement of the vortex.

Although the inner vortex core still is not well resolved at this data resolution, the simulated results from cycling 3DVAR with such extra information are quite promising as is shown in Fig. 18. The simulated track in the Q-GPS run has been improved as compared to the runs without the cycling approach (Fig. 8a). For example, the vortex center in this run has moved to a latitude slightly below 24°N at 36 h, which is closer to the observed position than in the no-GPS and GPS runs. The geometric distributions of the accumulated rainfalls during 0–24 and 24–48 h for the cycling run are presented in Figs. 18c,d (corresponding to Figs. 7c,d for the noncycling run GPS). The tendency of the observed intense rainfall in southwest Taiwan has been somewhat captured in this cycling run, for example, with the presence of a 50-mm contour in the southeast–northwest direction. This particular feature is completely missing in the noncycling GPS run and the no-GPS run. Compared with the observations in Fig. 2, the 24-h accumulated rainfall maximum (466 mm) to the northeast of Taiwan on the second day is better simulated, although not significantly. The intense rainfall is also more widespread in the cycling run compared to the GPS run associated with a more confined area. However, on the second day, the maximum accumulated rainfall (272 mm) over the southwestern slope base of the CMR is somewhat smaller than that in the GPS run (392 mm), and both are still far less than the observed (571 mm) at 23.5°N and 120.6°E. Thus, there are some gains and losses in terms of intense rainfall prediction in this cycling run in spite of the attendant best track later in the simulation. As indicated by the

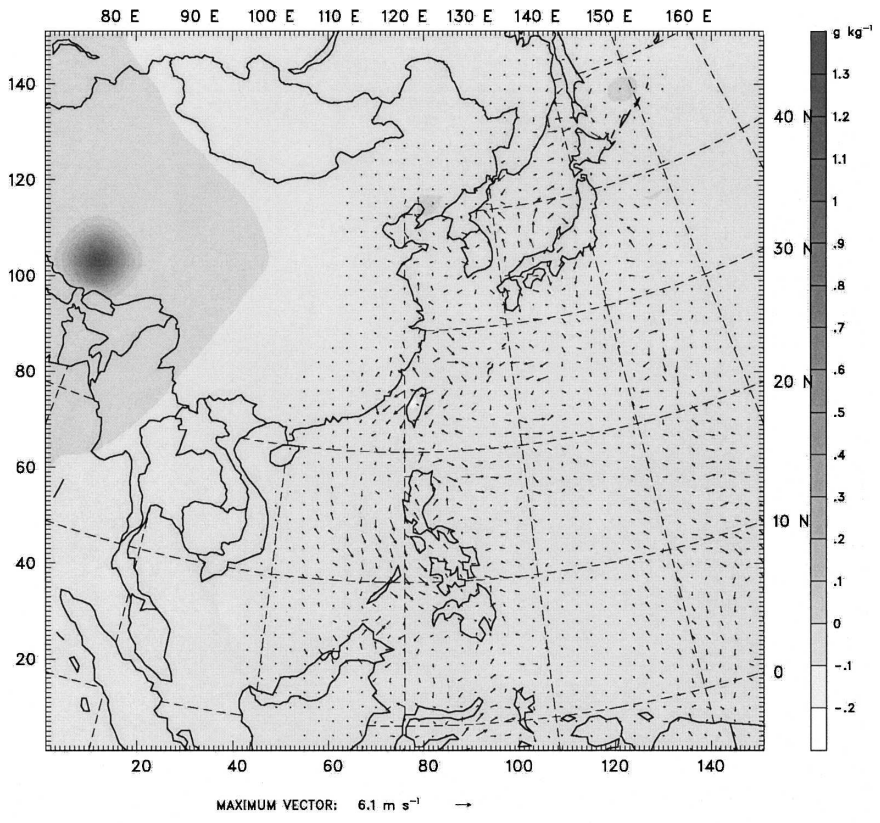

FIG. 17. The initial wind increments (m s^{-1}) and moisture increments (g kg^{-1}) at $\sigma = 0.870$ at 0800 UTC 16 Sep 2001 in the Q-GPS run with the QuikSCAT wind and one GPS refractivity sounding assimilated (see the text).

corresponding threat scores in Table 2, the prediction of accumulated rainfall on the second day (24–48 h) for this cycling run is considerably improved, especially for large thresholds. The results reiterate the positive impact of ingested wind observations on the prediction of accumulative rainfall, in particular, at later stages.

4. Conclusions

The present study utilizes three-dimensional variational data assimilation (3DVAR) analysis to ingest GPS refractivity data into model initial conditions for simulations of typhoons past Taiwan. Two recent typhoons were chosen for simulation: Typhoon Nari in September 2001 and Typhoon Nakri in July 2002. The GPS observations were taken from the currently operating CHAMP and SAC-C satellites that provide several refractivity profiles in the simulation domain near the initialization time. There are four (five) soundings that were assimilated into the initial conditions for Nari (Nakri). After 3DVAR assimilation, initial moisture increments from ingested GPS soundings show a maximum magnitude of 1.5 g kg^{-1} associated with the corresponding temperature increments of typically less than 0.2°C. Refractivity increments are less than 3% of the total refractivity, with variations similar to those of the moisture increments. This indicates that the increments from GPS refractivity contribute most to moisture, not temperature or pressure. Most of the moisture increments and temperature increments occur within an influential radius of 500–600 km of the occultation points.

The mesoscale model MM5 (version 3.5) is applied in this study to simulate typhoons with full physics including ice/graupel cloud microphysics. Three nested domains are used in the simulation with the finest 5-km resolution to resolve the steep Central Mountain Range (CMR) of about 4-km height in Taiwan. In the no-GPS run, the simulated Typhoon Nari consistently moves southwestward toward Taiwan but then exhibits a farther westward track along northwest Taiwan after landfall. With GPS refractivity assimilated, the simulated track is closer to the west coast. During landfall, the cloud convection associated with the intense vortex

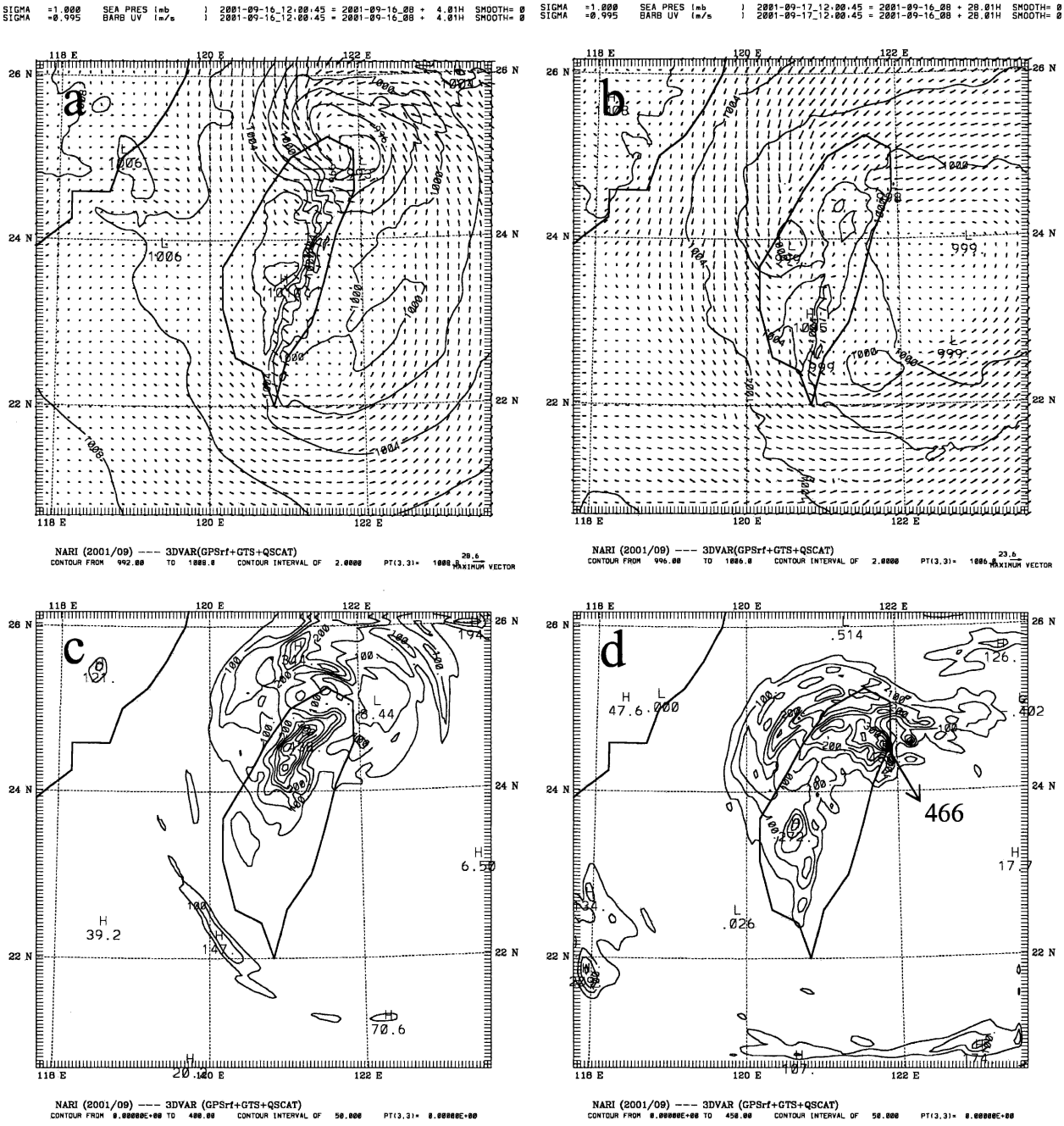

FIG. 18. (a) The simulated sea level pressure (hPa) and near-surface horizontal wind (m s^{-1}) in domain 3 in the Q-GPS run at 4 h (i.e., 1200 UTC 16 Sep) and (b) 28 h (i.e., 1200 UTC 17 Sep). (c) The simulated 24-h accumulated rainfalls (with a contour interval of 50 mm) in the first day in the Q-GPS run, and (d) as in (c) but on the second day.

core encounters the CMR and thus produces torrential rainfall along its northwestern slope. Both the no-GPS and GPS runs capture the observed feature of very intense rainfall over the southwestern slope base of the CMR later in the simulation, whereas the GPS run gives more intense and consistent maximum rainfall totals to the northeast and southwest of Taiwan. The prediction on 24-h accumulated rainfall is also improved in the GPS run compared to that in the no-GPS run, as verified by their threat scores.

The Nakri typhoon (actually a tropical cyclone) is rather weak at the initial time with five GPS soundings available for assimilation in the largest model domain. The simulated 24-h accumulated rainfalls in both the

GPS and no-GPS runs for Nakri in general are similar, but a more pronounced low is produced to the southeast of Taiwan in the GPS run, which results in more intense rainfall to the northeast of Taiwan as observed. The prediction of 24-h accumulated rainfall is also improved in the GPS run for Nakri, as indicated by the higher threat scores.

Although LEO satellites, such as GPS/MET, CHAMP, and SAC-C, can provide useful soundings on the thermodynamic variables, they lack the ability to measure wind. Wind information may play a dominant role in an assimilated vortex through geostrophic adjustment of the pressure field to the ingested wind field in low latitudes. To explore this possibility, cycling 3DVAR is performed to investigate the impact of additional wind information on the Nari simulation, which ingests observed QuikSCAT near-surface wind data from an oceanic swath covering the cyclone path. In the cycling run, the model prediction at a specific time is used as the first guess in the 3DVAR reinitialization with the wind observations. When such wind information is assimilated, the simulated track is further improved with a less slowdown of the vortex later in the simulation and therefore the prediction on accumulated rainfall is improved as well, as evidenced by higher threat scores against observations.

The relatively simpler operator by treating observed GPS refractivity as model local refractivity has been utilized in this study with a high-resolution (5 km) mesoscale model. The model simulation at later time is more susceptible to accumulative effects from small initial increments, as shown in the present study. With the input of several sounding observations over the ocean, the simulated results are more consistent with observations and undoubtedly support a positive impact of the data on the model simulation. Thus, the local refractivity operator is still reasonable and responsible in terms of the ability to blend useful observations into the simulation. On the other hand, the bending-angle operator is much more expensive than the local refractivity operator (Kuo et al. 2000), but it proves to be more accurate, particularly over the regions with strong horizontal gradients and in the lower troposphere where bending reaches a maximum (Zou et al. 1999). To account for the effects of observed nonlocal refractivity, Sokolovskiy et al. (2005) propose a more efficient but still accurate ray-tracing assimilation method for the integrated refractivity along a simplified ray trace. This effective scheme may be more feasible for real-time applications.

The current work on the assimilation of GPS occultation data will be extended to the new-generation model, the Weather Research and Forecasting (WRF) model, developed primarily at NCAR. WRF may also perform very well for hurricane track and rainfall predictions, as we found in other simulations with WRF for typhoons past Taiwan. The module of assimilation for local refractivity in MM5 3DVAR has been successfully implemented into WRF 3DVAR at NCAR and the nonlocal operator will also be developed with WRF shortly. The assimilation study with GPS data may also be extended to other weather phenomena such as meiyu fronts, cold-air outbreaks, and local convective storms. With the advent of plentiful COSMIC data, the impacts of the GPS soundings on numerical weather prediction can be investigated more thoroughly using WRF and MM5.

Acknowledgments. This study is supported by National Science Council in Taiwan under Grants NSC 93-2119-M-008-008-AP1 and NSC 93-2625-Z-008-015, and by National Space Program Office in Taiwan under Grant 93-NSPO(B)-RS3-FA07-01. Mr. W. Huang at NCAR provided some data used in this study. Ms. S.-Y. Chen and Ms. J.-R. Wang at NCU helped in simulation works.

REFERENCES

Anthes, R. A., C. Rocken, and Y.-H. Kuo, 2000: Application of COSMIC to meteorology and climate. *Terr. Atmos. Oceanic Sci.,* **11,** 115–156.

Barker, D., W. Huang, Y.-R. Guo, and A. Bourgeois, 2003: A three-dimensional variational (3DVAR) data assimilation system for use with MM5. NCAR Tech. Note NCAR/TN-453+STR, 68 pp.

Bevis, M., S. Businger, S. Chiswell, T. A. Herring, R. A. Anthes, C. Rocken, and R. H. Ware, 1994: GPS meteorology: Mapping zenith wet delays onto precipitable water. *J. Appl. Meteor.,* **33,** 379–386.

Courtier, P., and Coauthors, 1998: The ECMWF implementation of three dimensional variational (3DVAR) data assimilation. Part I: Formulation. *Quart. J. Roy. Meteor. Soc.,* **124,** 1783–1807.

Dudhia, J., 1993: A nonhydrostatic version of the Penn State–NCAR mesoscale model: Validation tests and simulation of an Atlantic cyclone and cold front. *Mon. Wea. Rev.,* **121,** 1493–1513.

Huang, C.-Y., Y.-H. Kuo, and W. Huang, 2002: Numerical simulations with MM5 3DVAR initialization. *Terr. Atmos. Oceanic Sci.,* **13,** 417–448.

Kuo, Y.-H., X. Zou, and W. Huang, 1997: The impact of GPS data on the prediction of an extratropical cyclone: An observing system simulation experiment. *J. Dyn. Atmos. Ocean,* **27,** 413–439.

——, S. V. Sokolovskiy, R. A. Anthes, and F. Vandenberghe, 2000: Assimilation of GPS radio occultation data for numerical weather prediction. *Terr. Atmos. Oceanic Sci.,* **11,** 157–186.

——, T.-K. Wee, S. Sokolovskiy, C. Rocken, W. Schreiner, D. Hunt, and R. A. Anthes, 2004: Inversion and error estimation

of GPS radio occultation data. *J. Meteor. Soc. Japan,* **82,** 507–531.

Liu, H., and X. Zou, 2003: Improvements to GPS radio occultation ray-tracing model and their impacts on assimilation of bending angle. *J. Geophys. Res.,* **108,** 4548, doi:10.1029/2002JD003160.

Lorenc, A. C., 1992: Iterative analysis using covariance functions and filters. *Quart. J. Roy. Meteor. Soc.,* **118,** 569–591.

Parrish, D., and J. Derber, 1992: The National Meteorological Center Spectral Statistical Interpolation analysis. *Mon. Wea. Rev.,* **120,** 1747–1763.

Rabier, F., A. Mc Nally, E. Anderson, P. Courtier, P. Unden, J. Eyre, A. Hollingworth, and F. Bouttier, 1997: The ECMWF implementation of three dimensional variational (3D-Var) data assimilation. Part II: Structure function. *Quart. J. Roy. Meteor. Soc.,* **123,** 27–52.

Sokolovskiy, S., 2001: Modeling and inverting radio occultation signals in the moist troposphere. *Radio Sci.*, **36,** 441–458.

——, C. Rocken, and A. Lowry, 2001: Use of GPS for estimation of bending angles of radio waves at low elevations. *Radio Sci.*, **36,** 473–482.

——, Y.-H. Kuo, and W. Wang, 2005: Assessing the accuracy of a linearized observation operator for assimilation of radio occulation data: Case simulations with a high-resolution weather model. *Mon. Wea. Rev.,* **133,** 2200–2212.

Vandenberghe, F., and Y.-H. Kuo, 1999: Introduction to the MM5 3DVAR data assimilation system: Theoretical basis. NCAR/MMM Tech. Doc., 38 pp.

Ware, R., and Coauthors, 1996: GPS soundings of the atmosphere from low earth orbit: Preliminary results. *Bull. Amer. Meteor. Soc.,* **77,** 19–40.

Zou, X., Y.-H. Kuo, and Y.-R. Guo, 1995: Assimilation of atmospheric radio refractivity using a nonhydrostatic adjoint model. *Mon. Wea. Rev.,* **123,** 2229–2249.

——, F. Vandenberghe, M. Pondeca, and Y.-H. Kuo, 1997: Introduction to the adjoint techniques and the MM5 adjoint modeling system. NCAR Tech. Note NCAR/TN-435-STR, 105 pp.

——, and Coauthors, 1999: A raytracing operator and its adjoint for the use of GPS/MET refraction angle measurements. *J. Geophys. Res.,* **104,** 22 301–22 318.

——, B. Wang, H. Liu, R. A. Anthes, T. Matsumura, and Y.-J. Zhu, 2000: Use of GPS/MET refraction angles in 3D variational analysis. *Quart. J. Roy. Meteor. Soc.,* **126,** 3013–3040.